2019

Computational Fluid Dynamics Models of Electromagnetic Levitation Experiments in Reduced Gravity

Gwendolyn Bracker

COMPUTATIONAL FLUID DYNAMICS MODELS OF ELECTROMAGNETIC LEVITATION EXPERIMENTS IN REDUCED GRAVITY

A Thesis Presented

By

GWENDOLYN P. BRACKER

Submitted to the Graduate School of the

University of Massachusetts Amherst in partial fulfillment

Of the requirements for the degree of

MASTER OF SCIENCE IN MECHANICAL ENGINEERING (M.S.M.E.)

September 2019

Mechanical Engineering

COMPUTATIONAL FLUID DYNAMICS MODELS OF ELECTROMAGNETIC LEVITATION EXPERIMENTS IN REDUCED GRAVITY

A Thesis Presented

By

GWENDOLYN P. BRACKER

Approved by:

_____
Robert W. Hyers, Chair

_____
Blair Perot, Member

_____
Wen Chen, Member

_____
Sundar Krishnamurty, Department Head
Mechanical & Industrial Engineering

ACKNOWLEDGEMENTS

First, I would like to thank my advisor, Prof. Robert W. Hyers for his guidance on the research project and mentorship during my time at Umass. Thank you for taking a chance on an unprepared-for-grad school undergraduate, I am grateful for the many opportunities to grow professionally, academically, and personally that you have provided.

I would also like to thank Prof. Blair Perot and Prof. Wen Chen for being exceptional teachers in the classes I have taken with each of them and for being members of my thesis committee.

I would like to thank my friends and family for their support throughout my education with special thanks to my parents for their support of my far-flung adventures.

I would like to thank Dr. Jennifer Carter for her mentorship and support during my undergraduate experience and for making the introduction to Prof. Hyers.

Elizabeth Hodges, thank you for embodying the values of PSR for both myself and our fellow sisters. I hope you continue to make the puzzle pieces to fit what you want on our joint adventure through the next phase of grad school.

Finally, I would like to blame Christian Oliver, my partner for this grand misadventure. Thank you for supporting me and believing in the dreams for which I did not have the courage. Without your encouragement and support, I would not have aspired for the graduate degrees I am working toward or been able to find the opportunities I have since pursued.

ABSTRACT

COMPUTATIONAL FLUID DYNAMICS MODELS OF ELECTROMAGNETIC LEVITATION EXPERIMENTS IN REDUCED GRAVITY

SEPTEMBER 2019

GWENDOLYN P. BRACKER, B.S.E., CASE WESTERN RESERVE UNIVERSITY

M.S.M.E., UNIVERSITY OF MASSACHUSETTS AMHERST

Directed by: Professor Robert W. Hyers

Electromagnetic levitation experiments provide a powerful tool that allows for the study of nucleation, solidification and growth in a containerless processing environment. Containerless processing allows for the study of reactive melts at elevated temperatures without chemical interactions or contamination from a container. Further, by removing the interface between the liquid and its container, this processing technique allows for greater access to the undercooled region for solidification studies. However, in these experiments it is important to understand the magnetohydrodynamic flow within the sample and the effects that this fluid flow has on the experiment.

A recent solidification study found that aluminum-nickel alloy sample have an unusual response of the growth rate of the solid to changes in undercooling. This alloy experienced a decrease in the growth velocity as the initial undercooling deepened, instead of the expected increase in solidification velocity with deepening undercoolings. Current work is exploring several different theories to explain this phenomenon. Distinguishing among these theories requires a comprehensive understanding of the behavior of the internal fluid flow. Our project, USTIP, has done flow modeling to

support this and multiple other collaborators on ISS-EML. The fluid flow models presented for the aluminum-nickel sample provide critical insights into the nature of the flow within the aluminum-nickel alloy experiments conducted in the ISS-EML facility. These models have found that for this sample the RNG k-ε model should be used with this sample at temperatures greater than 1800 K and the laminar flow model should be used at temperatures lower than 1600 K.

Other work in the ISS-EML, has studied the thermophysical properties of liquid germanium and has found the most recent measurements using oscillating drop techniques to have a discrepancy from the expected property measurements taken terrestrially. Investigating this discrepancy required the quantification of the velocity and characterization of the internal fluid flow in the drop. The models have found that the flow within the sample maintains turbulent behavior throughout cooling.

This thesis presents the analysis of the internal flow of four additional samples processed in the International Space Station Electromagnetic Levitation facility. These samples consist of the following alloys: $Ti_{39.5}Zr_{39.5}Ni_{21}$, $Cu_{50}Zr_{50}$, Vitreloy 106, and $Zr_{64}Ni_{36}$. Our collaborators work required the internal flow to be characterized and quantified for their work on solidification. In addition to quantifying the velocity of the flow, the Reynolds number was calculated to characterize the flow during processing. Additionally, the shear-strain rate was calculated for the flow during processing up to the recalescence of the melt.

TABLE OF CONTENTS

Page

LIST OF TABLES

LIST OF FIGURES

Figure Page

CHAPTER 1

INTRODUCTION

1.1 Purpose

The electromagnetic levitation (EML) program seeks to undertake various experiments and measurements on the fundamental properties, solidification behavior, and the effects of fluid flow on liquid metals. This family of projects is a long-standing collaboration of the National Aeronautics and Space Administration (NASA), the European Space Agency (ESA), the *Deutsches Zentrum für Luft- and Raumfahrt* (DLR, the German Center for Aerospace) and other national and international collaborators to investigate metals and the properties of liquid metals though containerless processing in an EML field. In these experiments the effects of magnetohydrodynamic flow are unique for each set of experiments. These effects can be indirectly studied through computational fluid dynamics models that relate the control voltage of the electromagnetic field to the flow within the drop.

This research is working to develop an improved understanding of the behavior, thermophysical properties, and solidification fundamentals of liquid metals. This improved understanding will benefit the current casting industry by allowing for better control of the microstructure through a more developed understanding of nucleation and phase selection. The improved property data will also allow for more accurate predictions of conditions during manufacturing processes. Further, this fundamental research is of critical importance to the developing additive manufacturing and aerospace industries where modeling is rapidly advancing and critical to producing reliable, certifiable parts

[1]–[3]. Current work aims to develop models of the process with the capacity to accurately predict the properties of the material and account for inhomogeneities based on the process [4]. Such models would allow for the certification and qualification of the manufacturing process and for the development of the ability to then produce parts based on the models.

This thesis seeks to contribute to the EML project by providing computational fluid dynamics (CFD) simulations of the flow within the liquid drops during the cooling process. These simulations are an important part of validation for measurements taken and provide a means to employ fluid velocity as an experimental parameter even though it cannot be measured directly. In the oscillating drop method, the viscosity and surface tension of the liquid can be measured during contactless processing; however this requires that the flow within the drop be laminar [5]. Additionally, other experiments utilize flow velocity as an experimental parameter and require the model to relate theory to direct observation [6]–[9].

1.2 Thesis Outline

Background information on the thesis is found in Chapter 2. This includes an overview of the larger overarching research program including the properties studied and measurements taken. Also included in Chapter 2 is a discussion of the relevance of computational fluid dynamics to the project, the oscillating drop method, fundamentals of computational fluid dynamics, the flow models used in the simulations, and calculations used to evaluate the qualitative and quantitative flow behavior. Chapter 3 discusses the overall set-up of the model including the boundary conditions. The preliminary work is presented in Chapter 4 and discusses the validation of model used to simulate flow within

the drop against prior work. As part of the preliminary work to this thesis, flow within two different samples was analyzed. Chapter 5 presents the results studying the flow in a germanium sample. Chapter 6 presents the results studying the flow in an aluminum-nickel alloy sample. Chapters 7-10 provides a detailed look at the flow in several other samples including titanium-zirconium-nickel, copper-zirconium, Vitreloy, and zirconium-nickel, respectively. Finally, overall conclusions are given in Chapter 11, and future work suggested in Chapter 12.

CHAPTER 2

BACKGROUND

2.1 Electromagnetic Levitation Project

The work presented in this thesis seeks to aid the larger family of EML projects. These projects are a long-term collaboration among NASA, ESA, the DLR, and others to study the melting, solidification, and liquid properties of conductive metals, alloys, and semiconductors [10]. Under the scope of the larger program are a wide array of experiments that seek to develop a better understanding of the fundamental properties and behaviors of liquid metals. The magnetohydrodynamic flow effects of the EML field are unique for each experiment due to variations in the electrical conductivity of the melt and the voltage applied to generate the EML field.

Fluid dynamics simulations are used to study the behavior of the flow within the samples during the cooling process and are an important part of the validation to measurements taken. Often the flow within the drops is not directly observable, so simulations can be used to relate the control voltage applied to the system to the velocity in the drop. Based on the properties of the liquid, the Reynolds number can be used to characterize the flow as laminar or turbulent. This characterization is important to understanding the results of the oscillating drop method, which requires laminar flow for valid results [5]. Additionally, other experiments utilize flow velocity as an experimental parameter and require the model to relate theory to direct observation [6]–[9], [11].

2.2 Oscillating Drop Method

The oscillating drop method allows for the containerless measurement of surface tension and viscosity and has been applied in EML and in many electrostatic levitation studies. The oscillating drop method assumed the liquid sample to be a force-free, inviscid droplet that behaves like a mechanical oscillator. The spring and dashpot system closely models the behavior exhibited by the samples observed in the EML project on the International Space Station (ISS) where the experiments for the project take place. In such a system, the levitation field is used to induce surface oscillations. Using the relations given by Rayleigh [5] and Lamb [12], the frequency of the oscillations is used to determine the surface tension and the damping of the oscillations is used to determine the viscosity of the liquid. These are given in the following equations:

$$f_l = \left(\frac{l(l-1)(l+2)\gamma}{3\pi m}\right)^{1/2} \quad (1)$$

$$\tau_l = \frac{\rho R_0^2}{(l-1)(2l+1)\mu} \quad (2)$$

Equation 1 is the relation used to determine the surface tension, γ, from the sample's mass, m, the natural frequency of the oscillations,f_l, and the mode of the oscillations, l. Equation 2 is used to determine the viscosity of the fluid, μ, using the damping coefficient, τ_l, the density, ρ, the radius of the sample, R_0, and the model of the oscillations, l.

To ensure that Rayleigh's assumption of inviscid behavior is satisfied, the following parameter, α^2, proportional to the quality factor, Q, of the mechanical oscillations. This parameter was developed to relate the relative effects of surface tension and viscosity. The value of α^2 should be greater than 59, as determined by Reid and Suryanarayana [13], [14]. This ensures that deviations of the natural frequency of the drop due to viscous effects are less than 1%. The calculation of α^2 is given in Equation 3.

$$\alpha^2 = \frac{(8\gamma\rho R_0)^{1/2}}{\mu} \quad (3)$$

The analyses of Rayleigh and Lamb assume that the amplitude of the oscillations is infinitesimal. For amplitudes up to about 1% change in polar radius, these assumptions are valid. Xiao, et. al., derived an empirical correction for larger amplitudes through a review of prior theoretical and experimental work on oscillations of droplets with finite amplitudes [15].

The oscillating drop method is extremely sensitive to liquid flow within the drop. Accurate viscosity measurements using this method require the internal flow to be laminar and that the internal flow not cause any energy dissipation to dampen the oscillations. Turbulence in the flow, allows for additional damping in the oscillations of the drop by allowing energy to be dissipated across the turbulent eddies. The energy dissipation results in damping times dominated by the turbulent dissipation rather than the liquid's inherent viscosity. [11]

The flow within the drop can be characterized very occasionally through the observation of tracer particles on the surface of the drop. This was observed in a palladium-silicon sample in EML on the space shuttle [16]. The tracer particles were observed to collect in the stagnation lines of the flow and were used to determine the laminar-turbulent transition. However, in the samples processed in the EML project, such tracer particles are rarely visible in the video to characterize the flow. Alternatively, computational fluid dynamics is used to calculate the flow velocity as a function of the thermophysical properties of the fluid and the control voltage of the applied electromagnetic field. Using this velocity and the known properties and the size of the sample, the Reynolds number is calculated to quantitatively characterize the flow behavior.

2.3 Fluid Flow and Solidification Studies

Convection of the fluid in the oscillating drop also affects the solidification and growth behavior of the drop. By using an applied force field the magnetohydrodynamics can be modeled to gain a deeper understanding of the influence that convection has on nucleation phenomena, growth kinetics, phase selection, and metastable phase formation [6].

In undercooled melts, the properties of the fluid flow affect the interactions between sub-critical nuclei within the drop [9] as is described by the coupled-flux nucleation model [7], [9], [17], [18]. In this model of nucleation diffusive and interfacial fluxes are considered when modeling the behavior of nuclei clusters. Each nuclei is surrounded by its diffusion field from which atoms are incorporated into the cluster and from which atoms dissolve back into the melt. These clusters and their diffusion fields are carried

along by the flow of the melt, as is shown in Figure 1, below. In non-uniform flows, like those that occur in EML, nuclei on adjacent streamlines move at different velocities. If the distance between clusters in the direction perpendicular to the flow is smaller than the diameter of the diffusion field, the diffusion fields will interact. Alternatively, if the distance between clusters in the direction normal to the flow is larger than the diameter of the diffusion field, the nuclei can pass each other without interacting [9]. In experiments, the shear-strain rate is important to calculate and ensure the diffusion fields around the nuclei are not interacting [7].

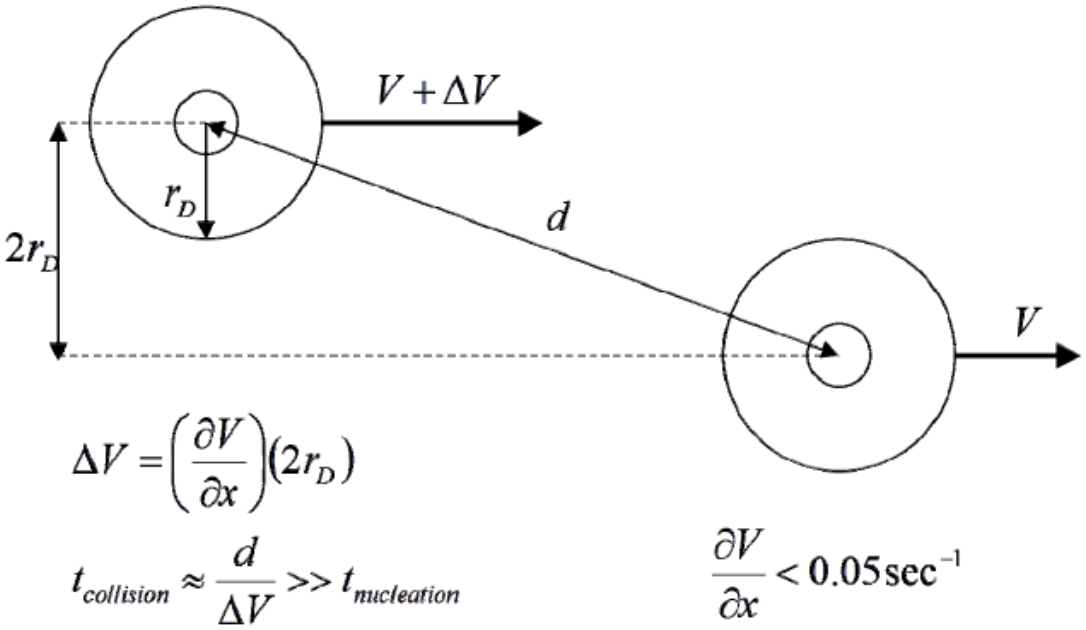

Figure 1: Coupled-flux nucleation model and the effects of fluid flow on the diffusion fields around subcritical nuclei [9], [19].

The nucleation of a stable, solid phase is also affected by the velocity of the fluid flow across growing dendrites. The authors theorize, when the velocity of the flow is sufficiently large, the primary dendrite deflects in the direction of the flow causing the secondary arms to collide with those of adjacent dendrites and form narrow crevices

between the dendrite arms, as is shown in Figure 2, [20], [21]. In accordance with classic nucleation theory, these crevices allow for a reduced critical nuclei volume and energy to nucleate a stable phase [22].

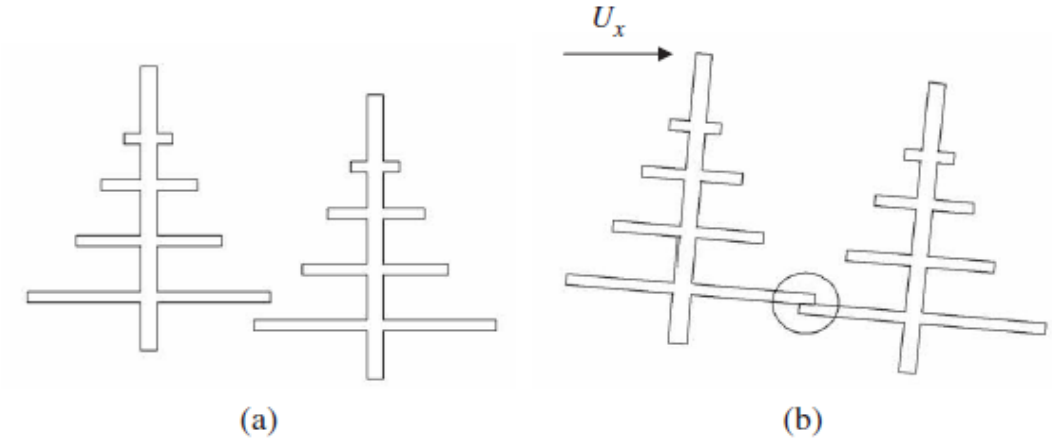

Figure 2: Depiction of growing dendrites. (a) There is no deflection of the dendrites and the secondary arms do not collide. (b) The convective velocity is strong enough to cause deflection and the secondary arms collide. Collision occurs within the circled region. [17], [18]

Current work also aims to explore the affect the fluid flow has on the growth of the solid phase into the liquid. It is typically expected that as the undercooling deepens, the velocity of the solidification front will increase [22]. The expected relationship between the growth rate and undercooling at the interface is shown for different interfaces in Figure 3 [19].

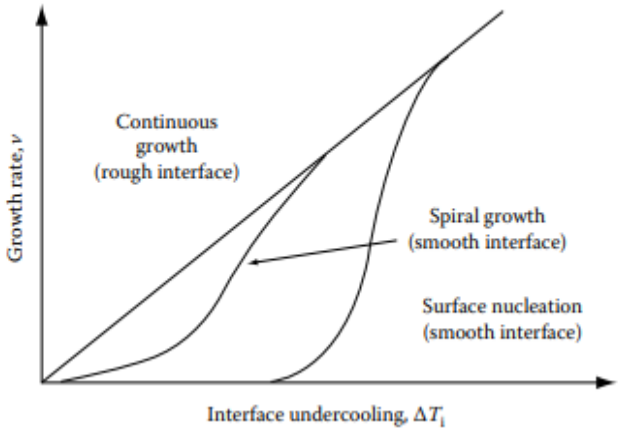

Figure 3: The influence of interface undercooling (ΔT_i) on growth rate for atomically rough and smooth interfaces. [19]

However, some undercooled liquids undergo a two-step solidification path, first forming a primary metastable solid and only afterward forming the stable solid secondary phase. When an alloy passes through a two-phase region during cooling, the growth rate of the stable solid is independent of the initial undercooling. The growth of primary phase is controlled by the initial undercooling and determines the fraction of solid particles in the melt. The second phase does not experience the initial undercooling but is instead undercooled by the melt. [8]. Other solidification phenomena include instances of double recalescence in which metastable solids are formed before the stable phase nucleates. However, neither of these scenarios fully explain the unusual growth behavior seen in recent work on aluminum-nickel alloys in which it was observed that the growth velocity decreases with increased undercooling for certain alloy compositions [23]. Figure 4 shows the results from studying the dendrite growth velocity as a function of undercooling under terrestrial and reduced gravity conditions over arrange of alloy compositions [20]. Further investigations are underway to explain this phenomenon including exploration of the effects of fluid flow.

The fluid flow is also a strong contributor to turbulent mixing in the liquid and determining the phase selection that can occur. At high flow velocities, turbulence causes sufficient mixing to approach the behavior of perfect mixing in the liquid which results in a more homogenous composition. Low flow velocities during growth result in mixing dominated by diffusion and produce a gradient composition based on the rejection of solute during solidification [22].

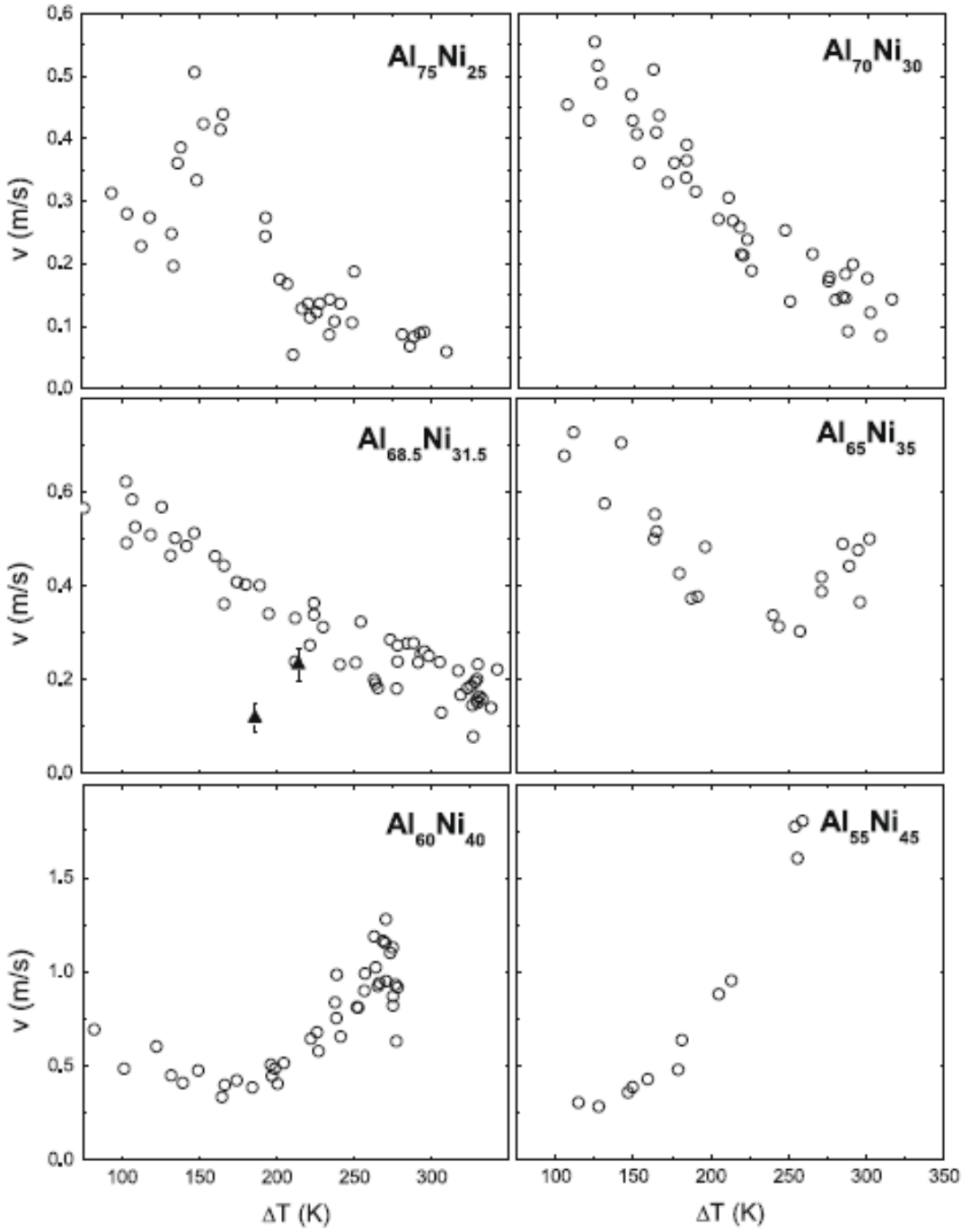

Figure 4: Anomalous dendrite growth in undercooled melts of Al-Ni alloys in relation to results obtained under terrestrial (open circles) and in reduced gravity (filled triangles). [20].

2.4 Computational Fluid Dynamics

Computational fluid dynamics (CFD) applies a set of numerical methods to approximate the solution to the differential equations used fluid dynamics and heat transfer problems. This is accomplished by discretizing the partial differential equations that define fluid mechanics into non-linear algebraic equations. These algebraic equations are solved using numerical methods with successive linear approximations. [24], [25]

2.4.1 Fundamental Governing Equations

The fundamental governing equations of fluid dynamics are the primary partial differential equations that CFD sets out to solve. For the purposes of this discussion of the fundamental governing equations, the nomenclature used is given in Table 1. The primary set includes the laws of conservation of mass, conservation of momentum, and conservation of energy with additional equations to account for any special phenomena, like turbulence.

Table 1: Nomenclature for the discussion of the fundamental governing equations of fluid dynamics

ρ	Density
t	Time
p	Pressure
μ	Viscosity
e	Energy
$\boldsymbol{V}$	Velocity in vector space
$\boldsymbol{f}$	Force in vector space
u_i	Velocity in cartesian coordinates
x_i	Cartesian coordinates
f_i	Force in cartesian coordinates
S_{ij}	Strain rate tensor
δ_{ij}	Kroneker delta-tensor
$\mathbf{q}$	Internal energy per unit mass
$\dot{Q}$	Rate of internal heat generation

The law of conservation of mass defines the systems such that mass cannot be created or destroyed and in its differential form it is often known as the continuity equation shown below in equation 4. In incompressible flows, ρ is assumed to be constant in each phase and equation 4 reduces to equation 5 [24]–[27].

$$\frac{\partial \rho}{\partial t} + \nabla \cdot (\rho \boldsymbol{V}) = 0 \tag{4}$$

$$\nabla \cdot \boldsymbol{V} = 0 \tag{5}$$

Newton's second law states that the change in the momentum of a body is equal to the net force acting upon it. When an ideal inviscid fluid is assumed, the momentum equation takes the form of Euler's equation given in equation 6 in which states that the mass per unit volume times acceleration is equal to the sum of the forces applied per unit volume.

$$\rho \frac{d\boldsymbol{V}}{dt} = -\nabla p + \rho \boldsymbol{f} \tag{6}$$

However, in fluid mechanics this system needs to account for both body forces acting directly on the mass of the fluid and surface forces acting on the surface of the fluid element. These are used to derive the Navier-Stokes equations as follows in equation 7. Under the assumption of an incompressible fluid with constant viscosity and defining the rate of strain tensor (equation 8), this reduces to equation 9 [24]–[27].

$$\rho \frac{Du_i}{Dt} = \rho f_i - \frac{\partial p}{\partial x_i} + \frac{\partial}{\partial x_j}\left[2\mu S_{ij} - \frac{2}{3}\mu(\nabla \cdot \boldsymbol{V})\delta_{ij}\right]$$

7

$$S_{ij} \equiv \frac{1}{2}\left(\frac{\partial u_i}{\partial x_j} + \frac{\partial u_j}{\partial x_i}\right)$$

8

$$\rho \frac{D\boldsymbol{V}}{Dt} = -\nabla p + \mu \nabla^2 \vec{\boldsymbol{V}} + \rho f$$

9

The final governing equation of fluid dynamics is the based on the first law of thermodynamics: energy is conserved. The equation for this using total energy is given in equation 10 [24], [25].

$$\rho \frac{De}{Dt} = -\nabla \cdot \boldsymbol{q} - \nabla \cdot (p\boldsymbol{V}) + \dot{Q} + \rho f \cdot \boldsymbol{V}$$

10

The solution to these equations requires a set of boundary conditions to reduce the number of unknowns in the system and dictate a particular solution. It is necessary to define one boundary condition or initial condition per variable per derivative taken to avoid unknown constants of integration. Often defining the system implies the boundary conditions used, for example how the fluid interacts with the wall is determined by the fluid. In an inviscid fluid, impermeable wall conditions are applied and the fluid can slip tangentially along the wall; while in a viscous system no-slip conditions are applied to the wall [24], [25]. Other boundary conditions that can be set include the domain for open boundaries such as an inlet or outlet for the fluid and restrictions on the computational

solution [24]. Details on the boundary conditions used in the model for this thesis are provided in Chapter 3: Model Set-Up.

2.4.2 Discretization Methods

There are several different approaches to discretizing the partial differential equations into algebraic equations. These approaches include finite element methods, finite volume methods and the finite difference method.

The finite element method can be used to solve the partial differential equations of fluid dynamics. This method divides the domain into cells or elements that form a grid. The finite element method allows for elements of be either triangular or quadrilateral and to be rectilinear or curved while the grid can be either structured or unstructured. This allows the finite element method to easily handle highly complicated geometries [25]. In solving fluid dynamics problems with the finite element method, the solution is assumed to have a given form. The functional space of the solution is determined by varying the function values between nodes in the grid and as a result of this the solution representation is strongly linked to the geometric representation of the domain [25]. The method by which finite element modeling finds the solution is by solving the integral form of the partial differential equation instead of directly solving the partial differential equations themselves. The most general method used to accomplish this is the method of weighted residuals. This method incorporates differential boundary conditions and allows for the easy construction of higher order methods [25]. Finally, the finite element method uses discrete equations that are constructed from the element level and are then assembled into the functions over the domain [25].

Finite volume methods can also be used to solve fluid dynamics problems by directly discretizing the integral form of the equations [24], [25]. In the finite volume method, the domain is divided into non-overlapping cells that cover the whole domain. These cells can be triangular or quadrilateral and form either a structured or unstructured grid. The finite volume method allows for the flexibility of the finite element method [25]. Nodes on the grid are then used to represent the interpolation structure, similar to finite element analysis. Nodes are often placed in a cell-centered arrangement; however, there are other arrangements of the nodes including cell-vertex schemes and staggered grid approaches [24], [25]. The finite volume method applies the conservation laws to predetermined nodes in the mesh [24], [25]. These volumes on which the conservation laws are applied can coincide with the cells but do not have to and can overlap and form the mesh of the grid [25]. By decoupling the volumes from the cells, the freedom in determine the function representing the flow field is increased. The finite volume method combines the flexibility of the finite element method with the flexibility of defining a discrete flow field as in the finite difference method [25]. However, the finite volume method has difficulty calculating the accurate derivatives because the computational grid is not necessarily orthogonal nor equally spaced, preventing the expansion of the derivatives using Taylor-series. There is no mechanism to convert higher order derivatives to lower ones, so the finite volume method is best suited to primitive variable problems where the viscous terms are not dominant. Further, curved cell boundaries are difficult to implement. As a result, cell boundaries are typically represented as straight and gridlines are piecewise straight; improved representation is possible but is complicated. The finite volume method is typically only second-order accurate [25].

The third major discretization system is the method of finite differences. This method is based on replacing the partial derivatives in the governing equations with algebraic quotients to develop a system of algebraic equations that can be used to solved the flow-field variables at specific, discrete grid points in the flow [25]. The computational grid covers the solution domain and its boundaries over both time and space. The time interval of the solution can have either uniform or variable step sizes, however the upper limit of Δt is set by requirements for accuracy and numerical stability of the system [24]. In the space domain, the grid spacing can be either constant to form a structured grid that is traditionally used in the finite difference method or can be nonuniform to form a clustered or stretched grid which allows for greater geometric flexibility in the solution [24]. The nodes of the system are placed at the intersections of the grid system and indexed to identify each grid point. The partial derivatives are approximated between the nodes using numerical methods such as a Taylor series expansion. Other more complex approximation schemes can be more accurate and allow for higher order differentiation for different problems.

In explicit schemes, the dependent variable is obtained from known results which allows for simple set-up and programing of a CFD model. However, explicit systems often require small time and space steps to maintain stability in the solution, which can result in long computation times. Implicit finite difference solutions are also possible and consist of an unknown expressed in terms of known and unknown variables. This results in a system of algebraic equations with unknown variables that can be solved for simultaneously. Implicit systems allow for greater stability and are often able to take fewer steps to solve a system and thus require less computation time; however, these

systems are complicated to set-up and program, require very large matrix manipulations at each time step. Additionally, implicit schemes often utilize larger time, or pseudo-time, steps which result in larger truncation errors and are more computationally expensive per step. [24], [25].

For the purposes of this project, ANSYS Fluent was used to execute the CFD analysis for the system and the software uses a finite volume discretization approach. ANSYS Fluent allows for one of two numerical methods to be used: a pressure-based solver developed for low-speed, incompressible flows and a density-based solver developed for high-speed, compressible flows. It should be noted that both methods have been expanded to operate for a wide range of flow conditions beyond their original design [28]. Using both methods, ANSYS Fluent solves the governing equations for mass, momentum, and energy conservation and other necessary scalars with a control volume technique. This technique divides the domain into discrete control volumes, then discretizes the governing equations over each control volume for the dependent variables, and finally linearizes the system to yield updated values of the dependent variables [28].

2.5 Flow Models

In studying the flow, it is important to characterize the flow behavior and match the models to the appropriate laminar or turbulent flow behavior. The can be quantitatively assessed by using the Reynolds number, Re, for the flow which is defined as a function of density (ρ), viscosity (μ), flow velocity (u), and length scale (L) as follows [26], [27]:

$$Re = \frac{\rho u L}{\mu}$$

11

At low Reynolds numbers, flows are dominated by laminar flow behavior. Laminar flow is characterized by smooth, sheet-like flow patterns [26]. Alternatively, at high Reynolds numbers, the flow is dominated by turbulent behavior which is characterized by chaotic eddy currents that redistribute the momentum of the flow and induces irregular mixing [24], [26].

While laminar flow is well modeled with the governing equations of fluid dynamics, turbulent flow requires modifications and additional calculations to the basic equations. Through the electromagnetic levitation project, a range of different models have been explored including enhanced-viscosity models, the k-ε model, and direct numerical simulations, but these models are not suitable to obtain realistic velocity field in the drop [29]. In the k-ε model, the effective turbulent kinematic viscosity is locally estimated via calculations of the turbulent kinetic energy and the turbulent rate of dissipation. With additional transport equations, empirical constants are applied to the system and assumed to be universal and geometry-independent [29]. However, work prior to that presented by Berry used the k-ε model to estimate the dynamic viscosity in levitated drops and while correctly showed a reduction in the turbulent eddy viscosity near the surface of the drop but also showed an incorrect increase in the turbulent eddy viscosity near the azimuthal axis and droplet center [29], [30].

Modifications to the k-ε model have greatly improves the accuracy of the simulations [29]. The renormalization group (RNG) method has become a commonly used modification and is the turbulent model used by ANSYS Fluent for these simulations [31]. The RNG k-ε model improves upon the standard k-ε model by adding an additional term to the turbulent dissipation equations, including the effect of swirl, analytically

calculating the turbulent Prandtl numbers, and analytically deriving the effective viscosity to make the method more accurate and reliable for a wider class of flows [31]. The RNG method uses dynamic scaling and invariance with iterated perturbation methods to re-evaluate the transport coefficients and equations [32]. This is done by iteratively averaging an infinitesimal band of small scale fluctuations until the viscosity becomes scale independent [29], [32]. This method can be applied to both high and low Reynolds number flows without requiring wall functions or additional constants in the governing equations while also allowing for variability in the Reynolds stresses over the domain [29], [32].

The turbulence models predict lower flow velocities and lower Reynolds numbers than are predicted by the laminar models. In the transitional region, this can result in the turbulence model predicting flow below the critical rate for turbulent flow; however, if the laminar model is characterized by a Reynolds number above the transition, the turbulent model should be used. For the simulations, it was determined by Berry that the RNG k-ε model is most applicable to the EML because it is most qualified for Reynolds numbers that are relatively low when compared to fully developed turbulent flows that are characterized by Reynolds numbers on the order of $10^4 – 10^5$. However, for the purposes of EML analysis, these comparatively low Reynolds number flows that are characterized by Reynolds numbers of several hundred to several thousand will be considered turbulent. These flows do demonstrate the chaos, mixing, and vorticity characteristic of turbulent flow. However, since the largest eddies are constrained by the free surface of the drop, the flow cannot reach fully-developed, isotropic turbulence.

Prior work has been done comparing the different turbulence models in levitated drops has found that the RNG k-ε model has excellent agreement with laminar models were expected. The RNG model is able to predict non-uniform turbulent eddy viscosity, as expected, and predict smaller, localized turbulent eddies [29]. More recent work was able to further validate this model by comparing the predicted convection velocity on the surface of the drop with the velocity of tracer particles on the surface of undercooled $Co_{16}Cu_{84}$. This work found that the predicted velocity was in excellent agreement with the observed experimental results of approximately 30 cm/s [33].

CHAPTER 3

MODEL SET-UP

ANSYS Fluent is a powerful computational fluid dynamics tool used to solve the fundamental governing equations of fluid flow. The models are set up to use the pressure-based solver, in a two-dimensional geometry with axisymmetric space and the solution is assumed to be at a steady time state. The mesh system used is shown in Figure 5.

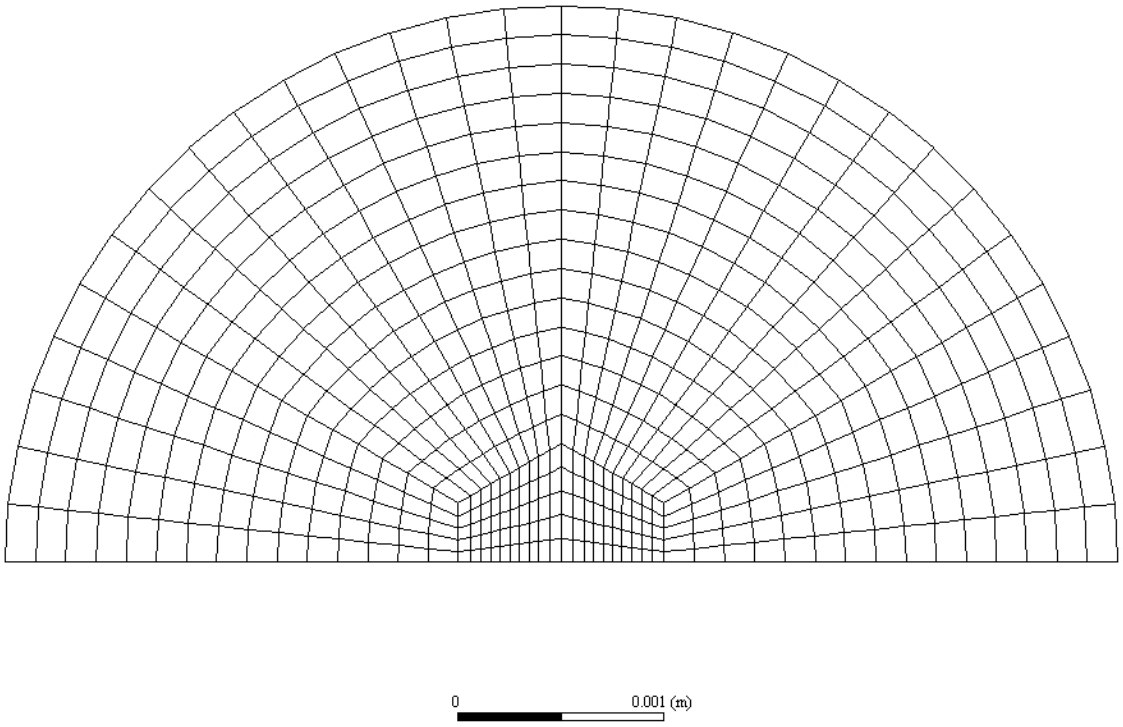

Figure 5: The structured mesh is shown above. This mesh includes 550 orthogonal cells.

The environment of the drop being modeled is a vacuum with an electromagnetic force field applied to the drop. The force field is determined based on the experimental parameters of the EML system: the geometry of the sample, conductivity of the sample, geometry of the levitation coils, the applied current and the applied frequency. A

preexisting program uses a volume integral to solve for the profile of the electromagnetic force field numerically [34], [35]. The force vectors are applied to the mesh in ANSYS Fluent using a User Defined Function (UDF).

There are several assumptions that define the computational boundary conditions that must be satisfied in the solution. First, the flow cannot cross the free surface of the drop, nor the symmetry axis. Additionally, the free surface of the drop is free of traction. Finally, the derivatives must be zero at the axis of symmetry to maintain symmetry at the boundary. With these boundary conditions applied to the system, the SIMPLE-Consistent algorithm, which increases the under relation to reach convergence more quickly, is used to solve the pressure-velocity coupling [36]. The gradient spatial discretization is done using the Green-Gauss Node Based method. The pressure spatial discretization is done using the Body Force Weighted method, while the momentum spatial discretization is done with the second order upwind system. When needed, a high order term relaxation can be used to reduce numerical instabilities in the solution.

CHAPTER 4

MODEL VALIDATION

The model was tested against both a recent experiment and a prior model. When validating a model against an experiment, it is important to compare both the results and the conditions of the experiment as experimental error can create unexpected conditions and inaccurate results. However, when validating a model against a model, it cannot be assumed that either model is correct. Both models should be judged for correctness and accuracy.

4.1 Experimental Validation

Using the computational model set-up described in Chapter 3: Model Set-Up, the model was validated against a cobalt-copper system tested in the ISS-EML facility [33]. In this experiment, the Co-Cu sample was levitated in EML field and melted using induction heating. This Co-Cu alloy was used in this experiment to take advantage of the metastable miscibility gap. With sufficient undercooling, the Co-Cu alloy experiences a liquid phase separation in which Co-rich particles can be traced to measure the convection velocity on the surface of the drop [33]. These Co-rich particles were then used as tracers to estimate the convection velocity on the surface of the drop near the equator. The model was validated using a mesh based on the detected geometry of the experiment with 987 nodes and 936 2D quadrilateral elements. The properties of molten copper at the test temperature were used as the properties of the liquid since in the molten state the Co-Cu becomes primarily 92 at% Cu-rich liquid with Co-rich particles [33]. As described above, ANSYS Fluent was used to solve the Naiver-Stokes equations with the electromagnetic forces calculated as part of a user defined function applied to the drop.

The results of the computational model and the experimentally observed flow velocity were both approximately 30 cm/s with a 7% discrepancy, which was comparable to the experimental uncertainty.

4.2 Validation against prior models

In addition to the experimental validation, the models were validated against a published model used to study convection in containerless processing of iron-chromium-nickel samples. This prior model was set-up to relate the current applied to the levitation coils and the flow velocity in the droplet. The model was tested against a test case in which 150 A was applied to the positioner coils and 0 A was applied to the heater coils. Using 7011 kg/m^3 as the density and 5.60 mPa·s for the viscosity, the prior model gave a maximum velocity of 1.9 cm/s, as can be seen in Figure 6 [7].

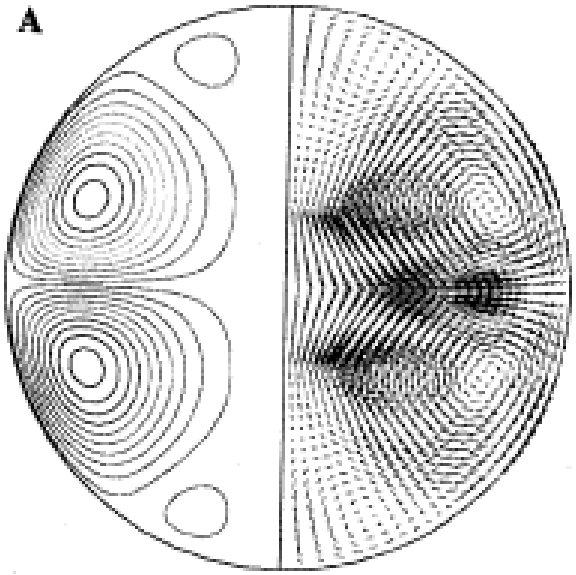

Figure 6: Fluid flow in positioner-dominated EML flow in FeCrNi droplets. The flow is driven by the 150A positioner current and 0 A heater current. It can be seen, that the flow is directed outward at the equator as a result of the distribution of the magnetic field [7]

Using these given properties and the EML field conditions from the prior model, the new model was tested. The current model predicted the maximum flow velocity in the drop to

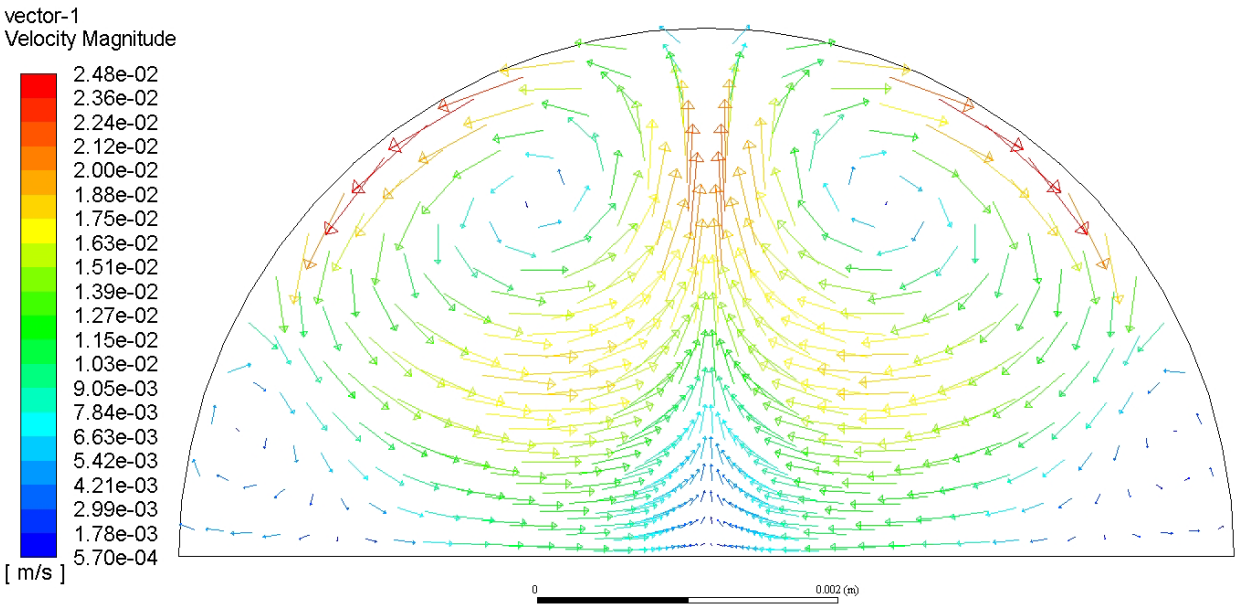

Figure 7: Results of applying the new model to the prior FeCrNi sample conditions. The maximum velocity is 2.48 cm/s and occurs along the surface of the drop.

be 2.48 cm/s, which can be seen Figure 7. The results give qualitative agreement to the prior published model. In both models the flow is fastest on the surface of the drop; however, current models report the velocity of the flow based on interpolations from nodes below the surface which may account for the discrepancies between the previously published model and the present iteration. Furthermore, the present model is based on the one reported in [30], which is the one validated against experiment.

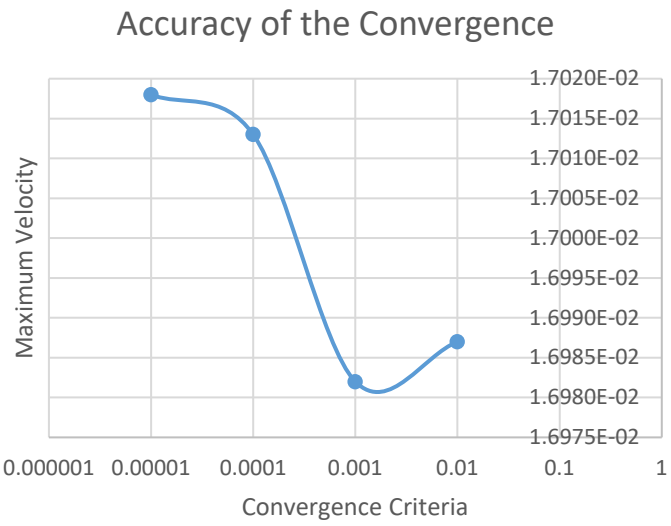

Figure 8: Plotted convergence of the solution

4.3 Convergence and mesh testing

The initial test case analysis was done using the mesh system shown Figure 5 which has 550 cells. The convergence of the solution was evaluated with respect to both the accuracy of the solution and the number of iterations. The solution value with the convergence requirement is plotted in Figure 8. At increasingly refined requirements for the convergence, the iterations required to reach the solution and the computation time increases. Using a tighter criterion for convergence increased the predicted maximum velocity by 0.2%. For the simulations presented here 0.001 was used as the convergence criterion.

In addition, new meshes were made and analyzed to explore the sensitivity of the mesh. Several of these are given in Figure 10. The meshes are distinguished from one another by the number of divisions along the radius of the drop with several key characteristics being shared across the different meshes. At the center of the mesh is an equilateral hexagon used to balance the requirement for elements of equal size and minimal distortion from 90° faces with the shape of the spherical drop. Radiating out from the hexagon are quadrilateral cells toward the surface of the drop. The radial mapping is more concentrated near the poles of the drop to better resolve the circulation loops in this region. Figure 9 shows the converged solution as a function of the number of nodes in the mesh.

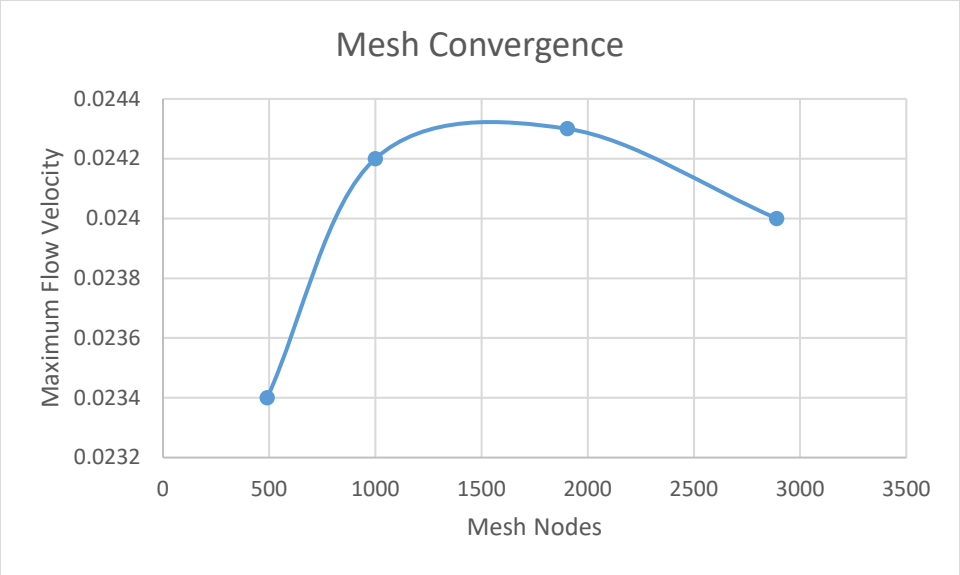

Figure 9: Solution convergence plotted against the number of nodes in the mesh.

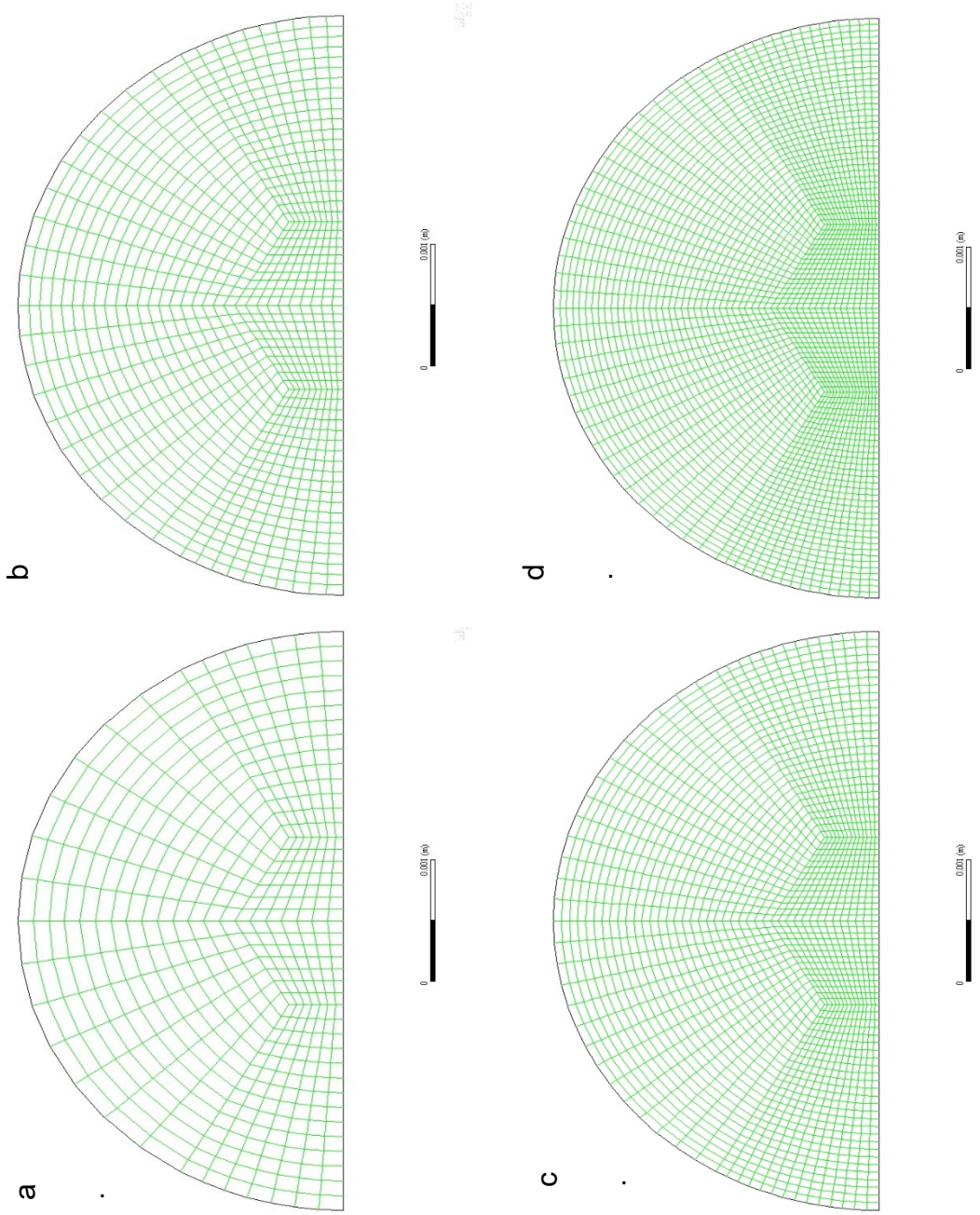

Figure 10: Meshes tested at various levels of refinement: a.) 20 divisions along the radius, b.) 30 divisions along the radius, c.) 40 divisions along the radius, d.) 50 divisions along the radius.

CHAPTER 5

ALUMINUM-NICKEL ALLOY

Sample 2 in batch 2.1 of the EML project is an $Al_{75}Ni_{25}$ alloy. This AlNi sample was part of a series of solidification studies in which a qualitative understanding of the internal flow behavior during cooling and solidification was needed. This sample is 527.24 mg and has a diameter of 6.5mm [37]. This alloy was expected to have a liquidus temperature at 1398K and a solidus temperature at 1132K [37], [38]. Our partners asked us to evaluate cycles 3 and 5 of those run on the $Al_{75}Ni_{25}$ sample on the ISS.

5.1 Alloy Properties

There are several properties that are important to modeling the flow within the drop as a function of the applied control voltage. These properties include the electrical conductivity of the liquid, the density of the liquid, and the viscosity of the liquid. The conductivity of the melt is used to determine the how strongly the electromagnetic field acts on the liquid sample. Prior work by Egry found the electrical conductivity of this liquid aluminum-nickel alloy to fit the equation given in Equation 12 [35]:

$$\sigma(T) = 10165 + 0.59(T - T_l) \quad [\Omega^{-1}m^{-1}] \tag{12}$$

Prior work done by Egry also studied the density of the liquid using containerless processing and a single color pyrometer calibrated to the liquidus temperature [35]. Using image analysis, the volume of the sample was measured with the assumption that the sample was axially symmetric. The density was then calculated using the known mass

and measured volume. The density as a function of temperature was then fit to the linear relationship given in Equation 13:

$$\rho(T) = 3.59 - 4.2x10^{-4}(T - T_l) \quad [g/cm^3] \tag{13}$$

The viscosity of the aluminum-nickel alloy was also measured in the prior work using an oscillating cup viscometer at several different temperatures. From the data taken, the behavior of the viscosity as a function of temperature was found and fit to a linear curve as follows in Equation 14 [38]:

$$\eta(T) = 7.94 - 0.0034 * T \quad [mPa\ s] \tag{14}$$

5.2 Results and Discussion

Using the model set-up described in Chapter 3: Model Set-Up, the fluid flow in the drop was modeled at the sample's maximum temperature during heating and throughout cooling. The applied, control voltage and temperature are plotted for these cycles in Figure 11. During heating the positioner and heater coils apply a combined electromagnetic force field to the drop that controls the drop's position and heats the sample through induction heating. The heating coils dominate the electromagnetic field

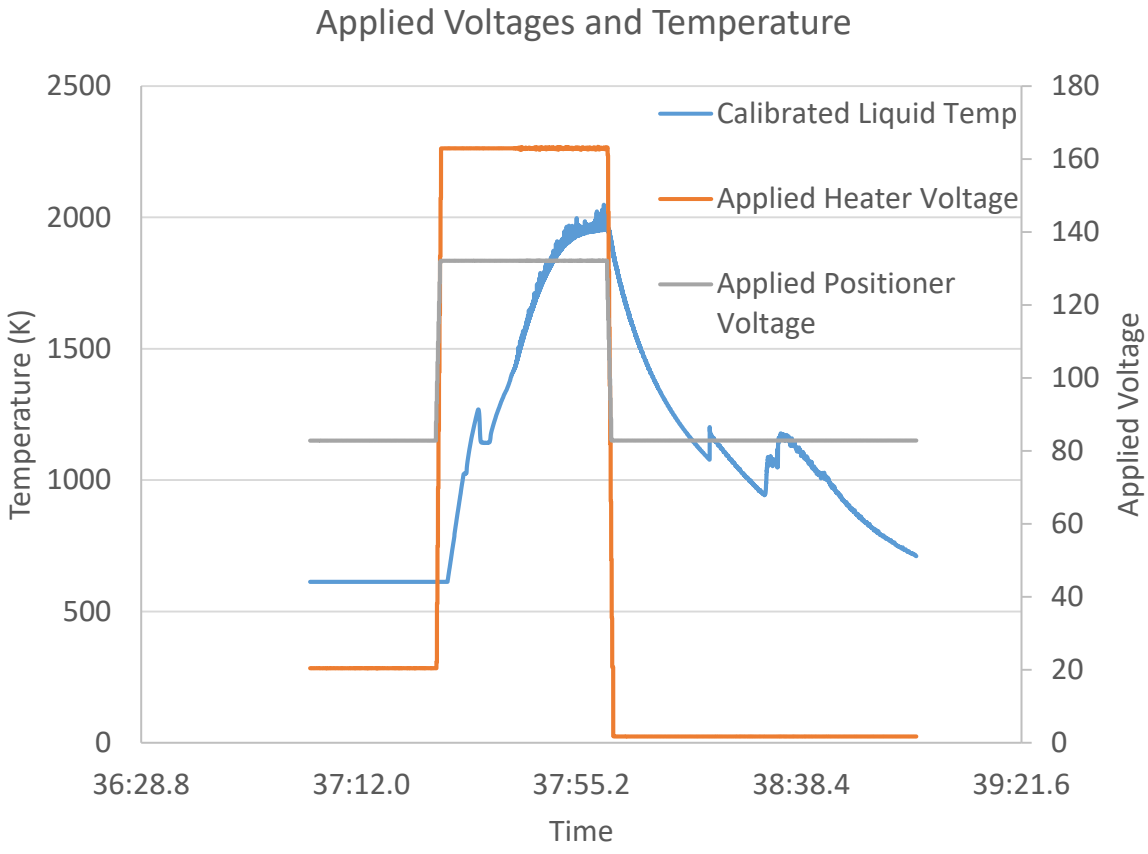

Figure 11: Positioner and heater voltages overlaid with the calibrated temperature of the AlNi drop during cycle 3 of the ISS MSL-EML tests during Batch 2.1. For both cycle 3 and cycle 5, the sample is heated and coils are reduced to allow the sample to cool after reaching peak temperature.

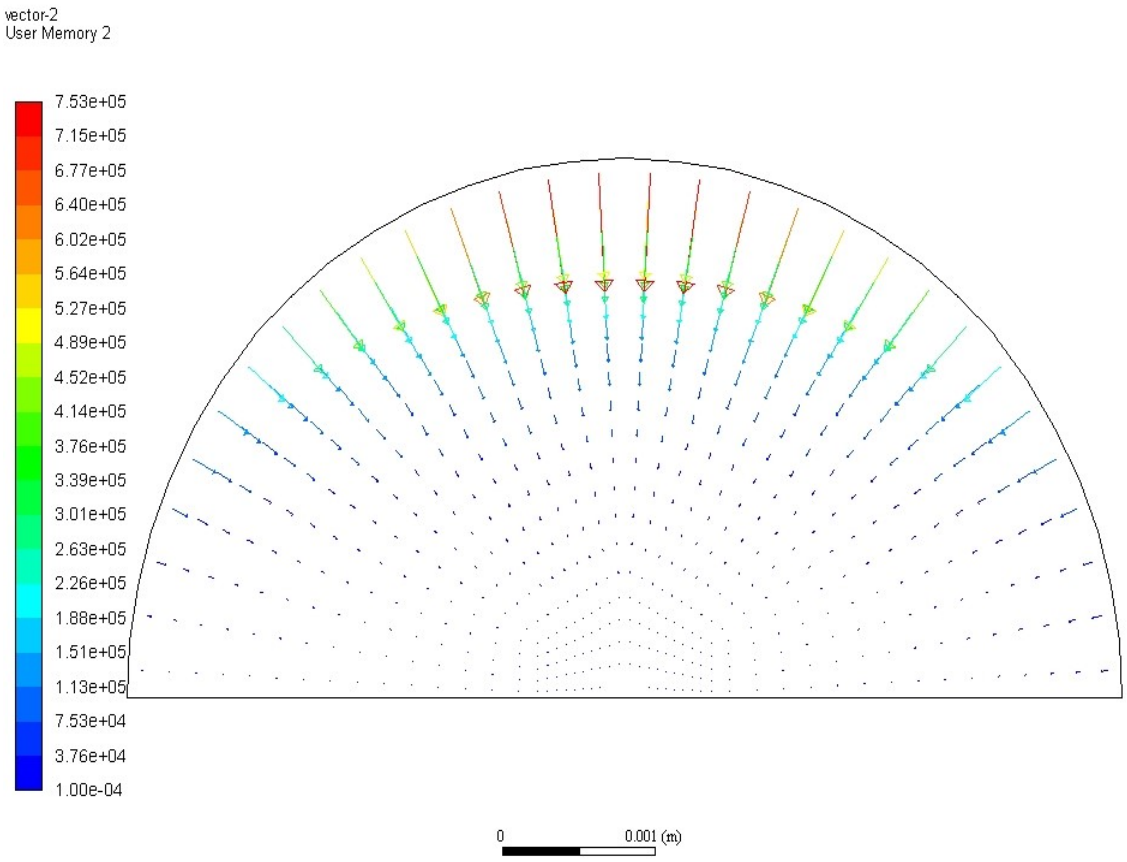

Figure 12: The EML field applied to the AlNi sample during the heating phase of cycle 3 and 5.

applied to the drop which acts as the primary driver of flow in the sample. The resulting field is shown in Figure 12. The aluminum-nickel alloy sample was analyzed in two cycles with different maximum temperatures. The first cycle modeled (Cycle 3) reaches a maximum temperature of 2050 K and the second cycle modeled (Cycle 5) reaches a maximum temperature of 1785 K.

These conditions were used to simulate the flow within the drop at the maximum temperature during heating to observe the maximum flow that occurred during the cycles. The resulting heater driven flow pattern is given in Figure 13. This flow pattern is consistent between the different cycles and different flow models. The maximum velocities resulting from these simulations are given in Table 2 and the calculated Reynolds numbers are given in Table 3. The high Reynolds numbers indicate that under these conditions the flow is highly turbulent.

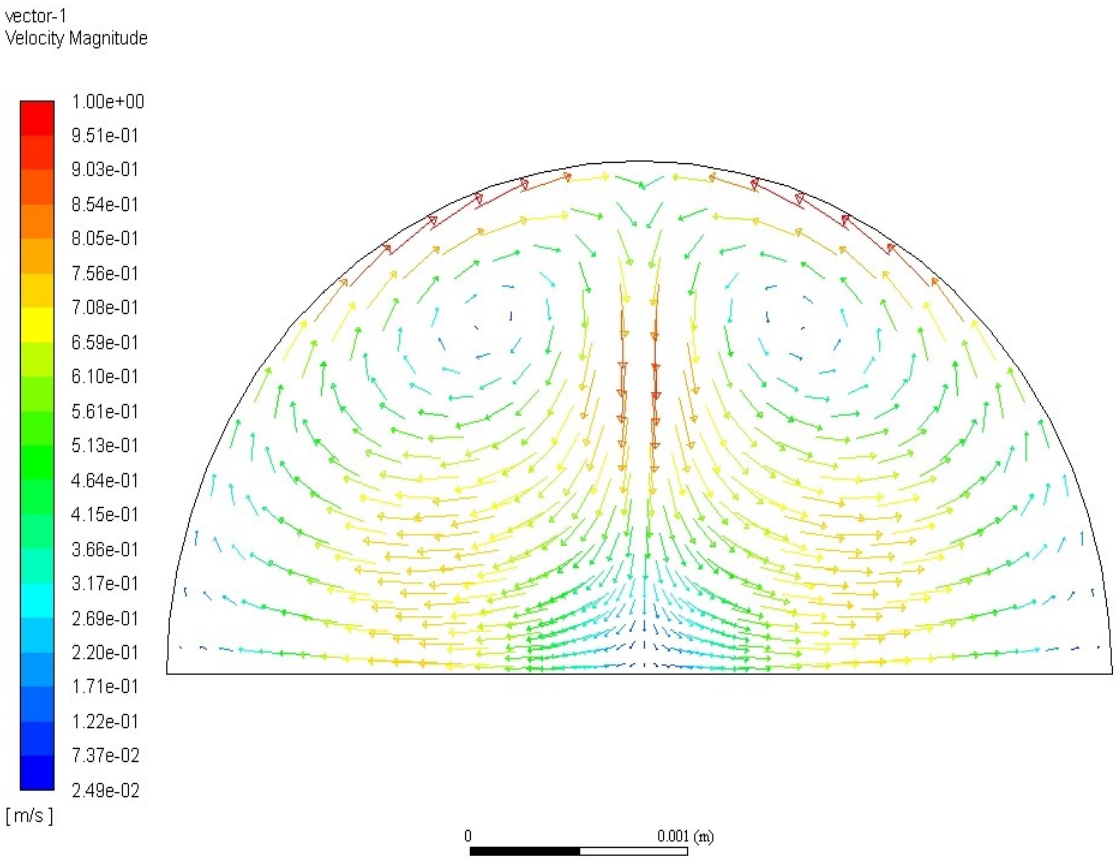

Figure 13: Heater driven fluid flow in the AlNi sample. This shows the flow model calculated using the laminar flow model, heater dominated EML field, and the liquid is assumed to be at 2050K. This flow pattern is consistent across AlNi heating conditions.

Table 2: Modeled maximum flow velocities for cycle 3 and cycle 5.

	Cycle 3	Cycle 5
Cycle High Temperature	2050K	1785K
Laminar Model	1.00 m/s	0.739 m/s
RNG k-ε Turbulence Model	0.449 m/s	0.432 m/s

Table 3: Reynolds numbers calculated for the maximum flow under heating.

	Cycle 3	Cycle 5
Cycle High Temperature	2050K	1785K
Laminar Model	22200	8670
RNG k-ε Turbulence Model	9990	5070

During cooling, the control voltage on the heater coil is reduced to zero and the control voltage for the positioner coil is reduced. The reduced electromagnetic field during cooling is given in Figure 14. In Cycle 3, the sample cooled and recalesced at 1077 K while cycle 5 experienced its recalescence at approximately 1150 K. The positioner driven flow that occurs during cooling and immediately prior to recalescence is shown Figure 15. The models of the flow prior to recalescence were analyzed for both cycles

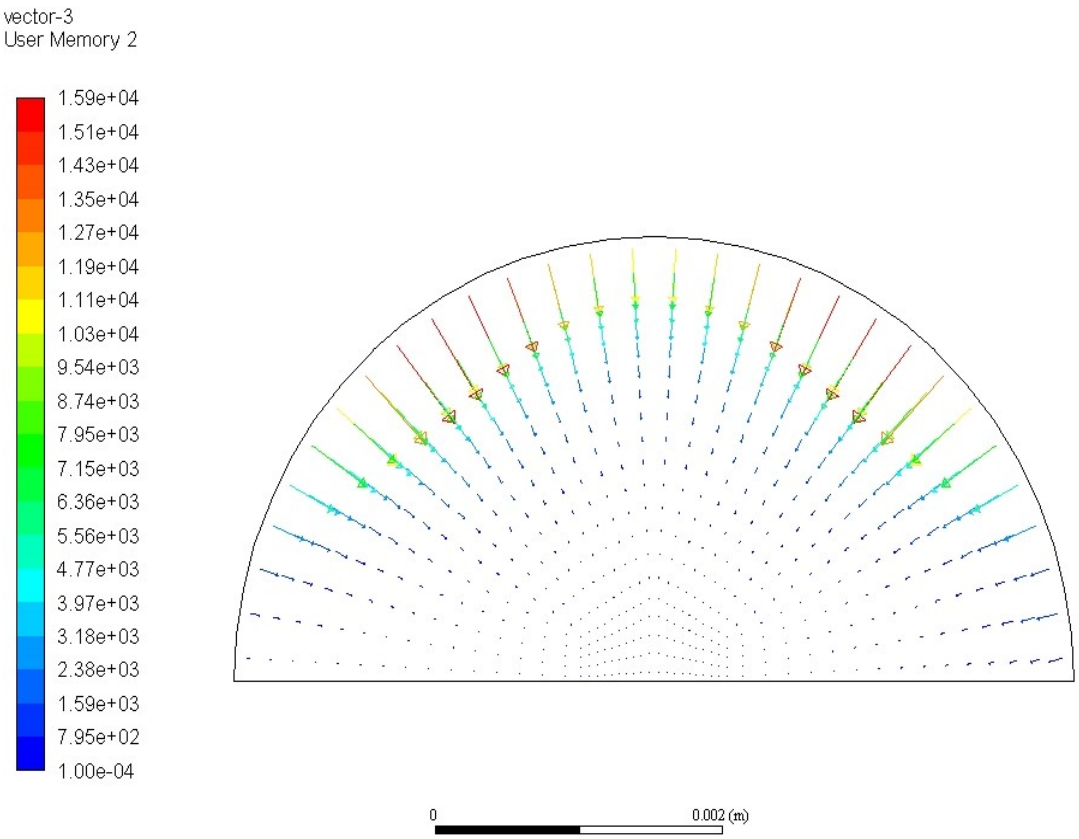

Figure 14: The positioner-dominated electromagnetic field is shown. The heater voltage is zero V and the positioner voltage is 9.7 V. This field is applied to the drop during the entire cooling phase of the cycles.

using the laminar model and RNG k-ε turbulence model. The calculated maximum flow results are given in Table 4 and the calculated Reynolds numbers for the flow are given in Table 5. Under both models the Reynolds numbers are well below 600, which indicates that the flow is likely laminar immediately prior to recalescence.

Table 4: Maximum flow velocity calculated in the drop under positioner dominated flow immediately prior to recalescence.

	Cycle 3	Cycle 5
Cycle Recalescence Temperature	1077K	1150K
Laminar Model	0.0530 m/s	0.0545 m/s
RNG k-ε Turbulence Model	0.0390 m/s	0.0395 m/s

Table 5: Reynolds numbers calculated to characterize the flow in the EML drops immediately prior to recalescence under positioner dominated flow.

	Cycle 3	Cycle 5
Cycle Recalescence Temperature	1077K	1150K
Laminar Model	300	325
RNG k-ε Turbulence Model	220	236

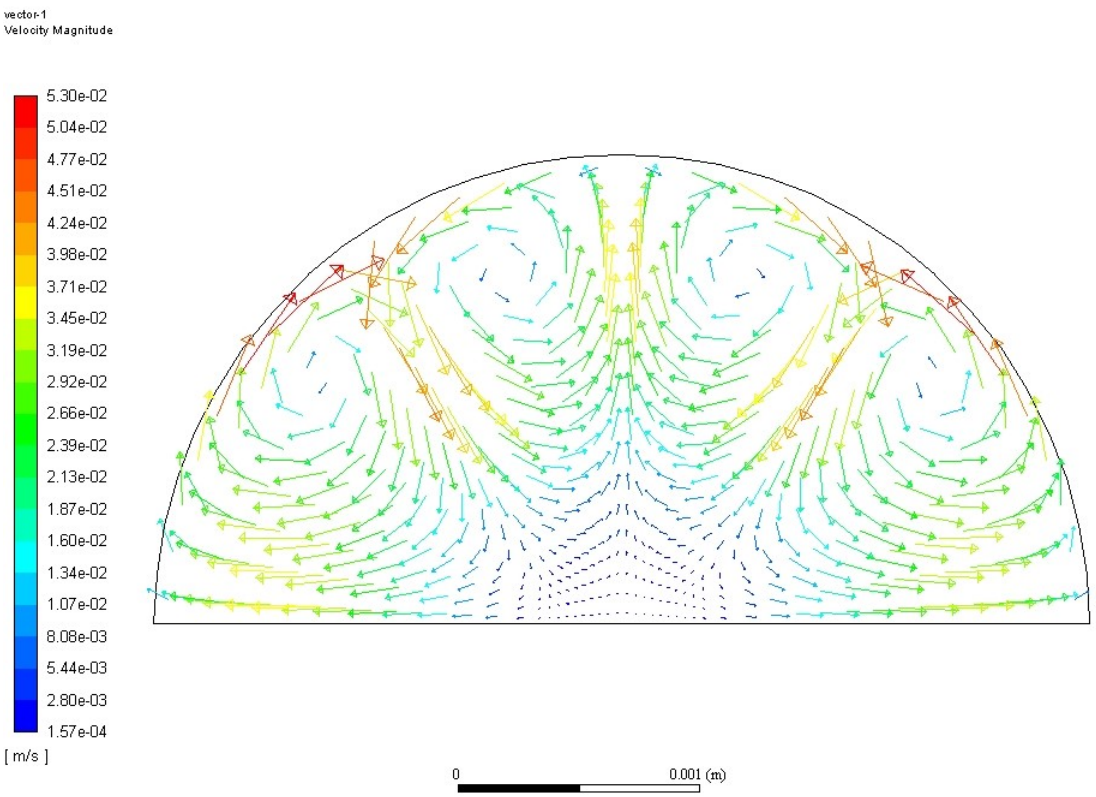

Figure 15: This is the fluid flow pattern for positioner dominated flow that occurs during the cooling phase of the cycle. This particular pattern is calculated from the laminar flow model in a positioner dominated EML field. The properties of the liquid were calculated using 1077K as the temperature.

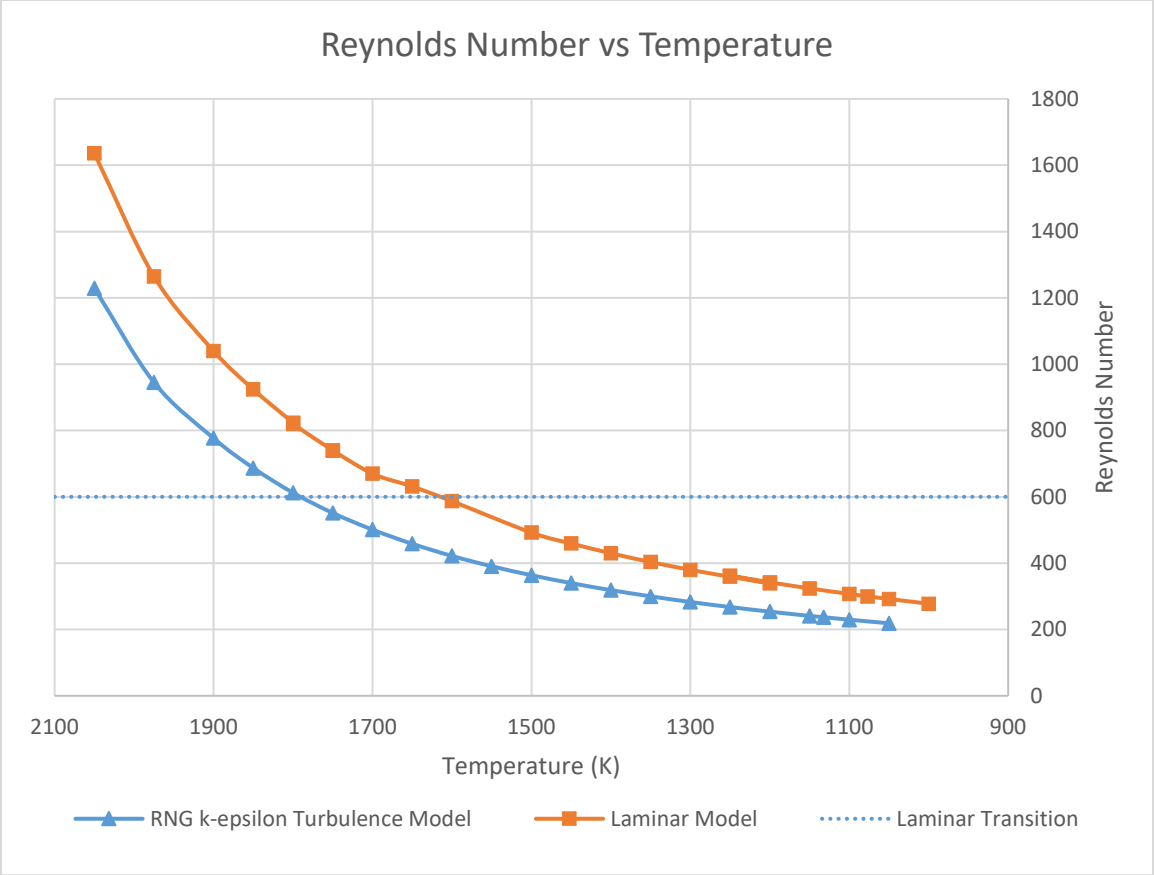

Figure 16: Reynolds numbers vs temperature of the molten sample during cooling. Above Reynolds numbers of about 600, shown with a dotted line, [16], the flow will be turbulent and the curved marked by triangles is applicable. Below this value the flow will be laminar, and the curve marked by the squares applies.

In addition to the maximum and minimum flow conditions of the cycles, the flow was also analyzed using the laminar and turbulent flow models over a range of different temperature conditions. Laminar flow models were evaluated across the temperature range. Using the laminar flow model, the Reynolds number for the flow increased above 600 at temperatures slightly higher than 1600K. This indicates that the laminar-turbulent transition is occurred above 1600K. At higher temperatures, the RNG k- ε turbulence model was used to estimate the flow behavior. The relationship between the temperature

and the Reynolds numbers for the different flow models is shown in Figure 16. These models used the thermophysical properties as a function of temperature to determine the maximum velocity within the drop at the given temperature. These values were then used to calculate the Reynolds number describing the flow.

5.3 Conclusion

Though the fluid flow models run on the aluminum-nickel alloy sample, an improved understanding of the flow during cooling and solidification was gained. In both Cycle 3 and Cycle 5, the highest temperatures of the cycles were modeled to display clear turbulent behavior. However, it is clear at the time of recalescence the flow transitions to a laminar behavior model. Based on previous work, the laminar-turbulent transition has been shown to occur near a Reynolds number of 600. Lacking clear video evidence of the behavior of the flow in the sample, these simulations provide the only insight into the nature of the flow.

The RNG k-ε model should be used when the Reynolds number is greater than 600, which corresponds to temperatures greater than 1600 K. Laminar flow models should be used when the Reynolds numbers for the flow is less than 600, which corresponds to temperatures less than 1600K.

CHAPTER 6

GERMANIUM

6.1 Experiment Overview

As part of the ISS-EML experiments, the thermophysical properties of liquid germanium were observed to correlate changes in the X-ray structure factor along with changes in properties to possible phase transitions proposed in supercooled silicon [37]. The antimony-doped germanium sample was processed as part of batch 2.1 in the ISS-EML. The 8mm diameter sphere sample consists of germanium doped with antimony at a

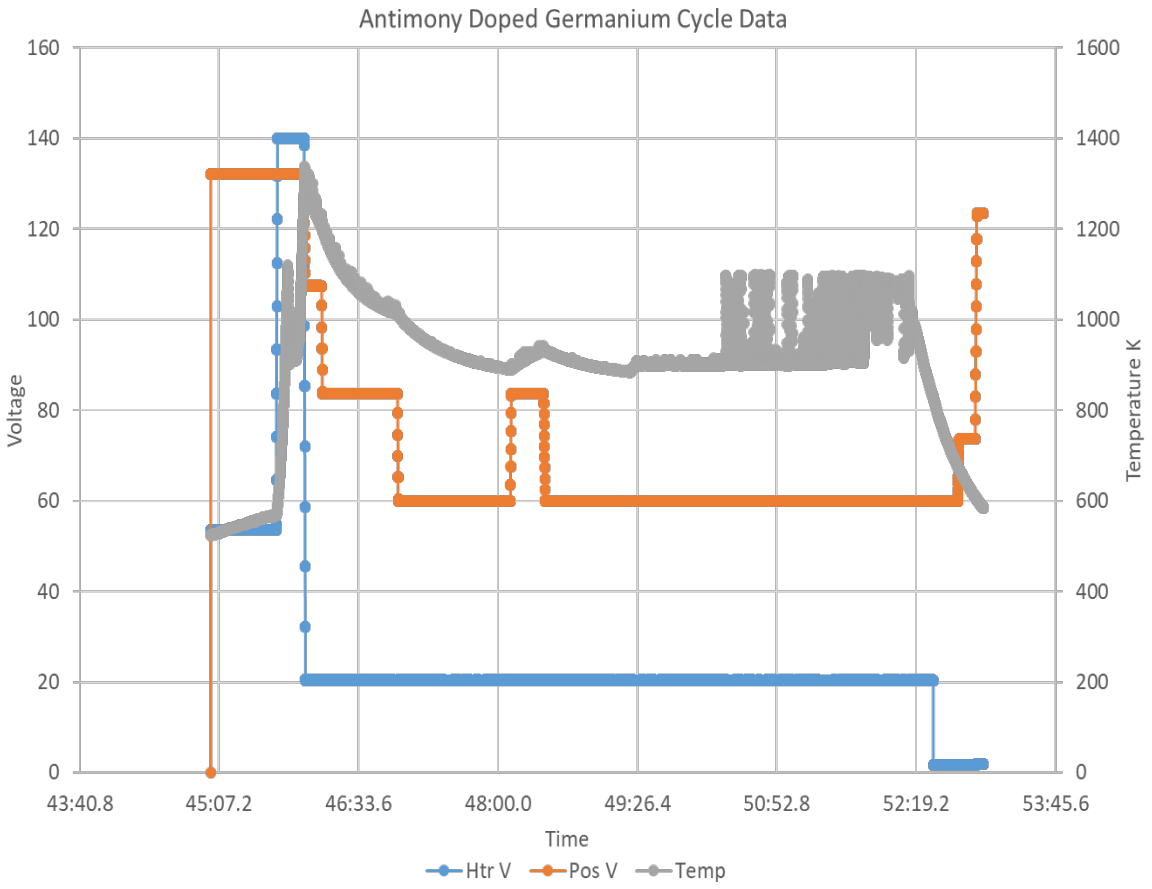

Figure 17: Temperature and control voltage data gathered during the doped germanium cycle.

concentration of $10^{19}/cm^3$. It was melted and oscillations were induced to study the properties of the liquid germanium; after which the sample was allowed to cool. The sample temperature, as measured by the pyrometer, plotted with the control voltages of the heater and positioner coil is given in Figure 17.

During the cycle oxide rafts are visible floating on the surface of the drop and provided an opportunity to qualitatively observe the behavior of the flow. The oxide rafts get caught in the stagnation lines of the flow. If the flow were to be laminar in the drop, the oxide rafts would have followed stable, linear patterns though the droplet. However, when the flow is turbulent, these rafts reflect the turbulent behavior of the flow and display a chaotic motion. This chaotic motion of the oxide rafts is seen throughout the video

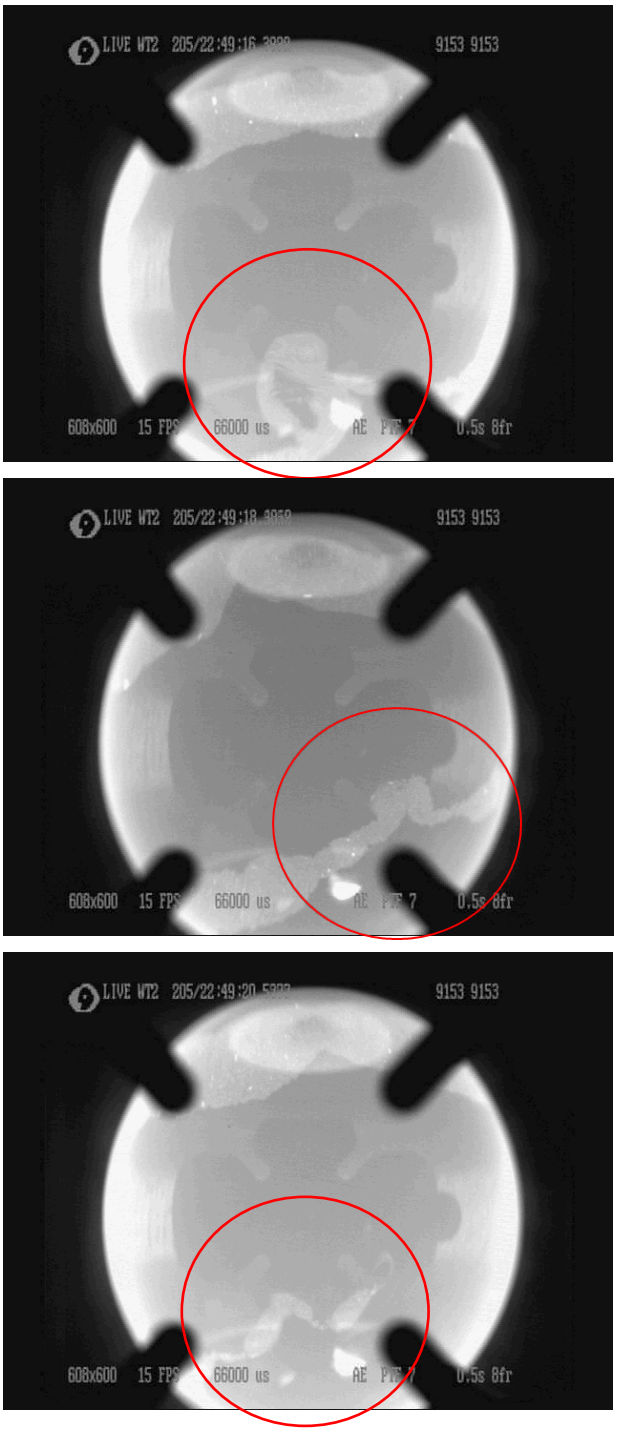

Figure 18: A-C: During cooling, the germanium sample displayed clear turbulent behavior that can be observed through the movement of the oxide rafts on the surface of the drop.

of the processing cycle and suggests that the flow within the drop is turbulent over the observation period. Shown in Figure 18 A-C is a series of images of the oxide rafts shortly before recalescence, when the temperature of the drop is at its lowest temperature. The behavior reflected here illustrates the chaotic motion that would be expected from turbulent flow. This turbulent response to the EML field is surprising because typical positioner-driven flow is generally laminar and undercooled samples are usually laminar; however, the kinematic viscosity of germanium is several orders of magnitude lower than that of other samples studied in EML. The lower kinematic viscosity is thought to be the cause of the high levels of turbulence observed in the sample.

6.2 Material Properties

As with the aluminum-nickel sample, the conductivity, density and viscosity are all necessary to model the flow within the drop. The electrical conductivity is necessary to determine the applied electromagnetic field to the drop. The conductivity of liquid germanium has been measured to be 1.52×10^6 $\Omega^{-1}m^{-1}$ at 1250 K using a modified oscillating coil system [39]. The high conductivity of the melt allows for the sample to be levitated and heated using the electromagnetic field.

The density of the molten germanium is important to solve the fluid flow equations in the simulations. Historical work has measured the density of liquid germanium as a function of temperature according to the following relationship [40]:

$$\rho_{liq} = (5.49 * 10^3) - 0.49(T - T_m) \quad (15)$$

More recent work has measured the density and thermal expansion of pure liquid germanium using contactless processing methods in microgravity. In Luo's study of

contactless processing of SiGe-melts, the density of pure, liquid germanium was measured to be 5570 kg/m^3 at 937°C and the volumetric thermal expansion was observed to be 10.1x10^{-5} °C^{-1} [41].

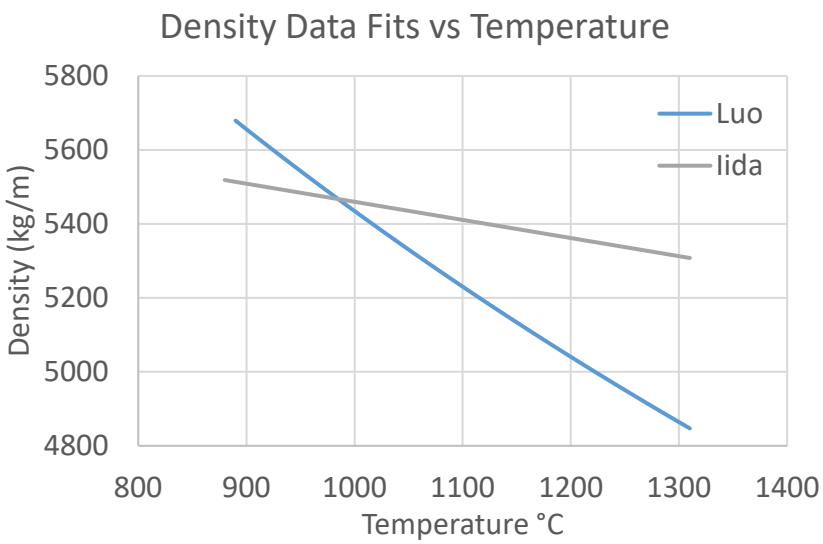

Figure 19: Comparing density models from different sources.

Comparing the observations in the parabolic flight experiment and the historical measurements, there is a 2.3% difference in density at the temperature of interest. For the purposes of these models, this is an acceptable error. In creeping flow at steady state, the density has no effect on the velocity of the fluid. In fast flows where the convective term is large, the convective term scales with the constant force. As a result, the velocity scales with the square root of the reciprocal of the density. Applying our given variation of 2.3%, this would be expected to yield a 1.1% difference in the velocity of the system.

The viscosity is a critical material property to determine how the flow will respond to the force of the electromagnetic field and the magnitude of the flow velocity. The viscosity of liquid germanium has been measured by multiple sources [41]–[43]. In recent experiments on the ISS, the viscosity of liquid germanium was measured to be 2.9 mPa-s based on the oscillating drop method [42]. However, this measured viscosity is significantly lower than that of previous parabolic flight experiments using the same

oscillating drop method. In the parabolic flight experiments, the viscosity was measured as a function of the damping rate of the oscillations and the data was fit to an Arrhenius relation [41]:

$$\eta = \eta_o e^{\left(\frac{E_A}{kT}\right)} \quad (16)$$

In which the viscosity at the high temperature limit, η_0, is given as 5 mPa s and the activation energy is given to be about 90-100 meV at high temperatures. Based on this, this viscosity at our target temperature would be expected to be between 12.4 and 13.6 mPa-s [41].

This viscosity of liquid germanium has also been measured by Gruner, et al., using the rotating cup method [43]. This method is less susceptible to inducing turbulent flow that would dampen the oscillation and provide erroneous results. Furthermore, any experimental problems due to secondary or turbulent flows would increase the apparent viscosity, so the measured value is a maximum. Gruner found that the Arrhenius-law could be applied to the measurements of viscosity. The measured asymptotic viscosity for undoped germanium was given as 0.206 mPa-s with an activation energy as 7.60 kJ/mol [43]. Based on this viscosity fit, it would be expected that at the temperature of recalescence, the viscosity of the drop would be 0.455 mPa-s.

The value for the viscosity using Gruner's fit is an order of magnitude lower than that reported by the ISS-EML experiments and is two orders of magnitude lower than the viscosity reported in the parabolic flight experiments [41]–[43]. However, the measurement method is less susceptible to errors due to turbulence which is expected in

the drop based on the video of the experiment. Additionally, estimates taken from prior measurements on liquid silicon, which is in the same period of the periodic table and has the same electron structure, suggest that the viscosity should be close to the range of 0.49 and 0.90 mPa-s [44]–[46].

6.3 Model Results

The flow conditions in the droplet were modeled at the maximum temperature achieved by the liquid metal to determine the maximum flow velocity achieved in the drop and to characterize the flow. These conditions occur during the heater driven flow immediately before the current applied to the heater coils and positioner coils is reduced and the sample is allowed to cool. The electromagnetic field applied to the drop let is

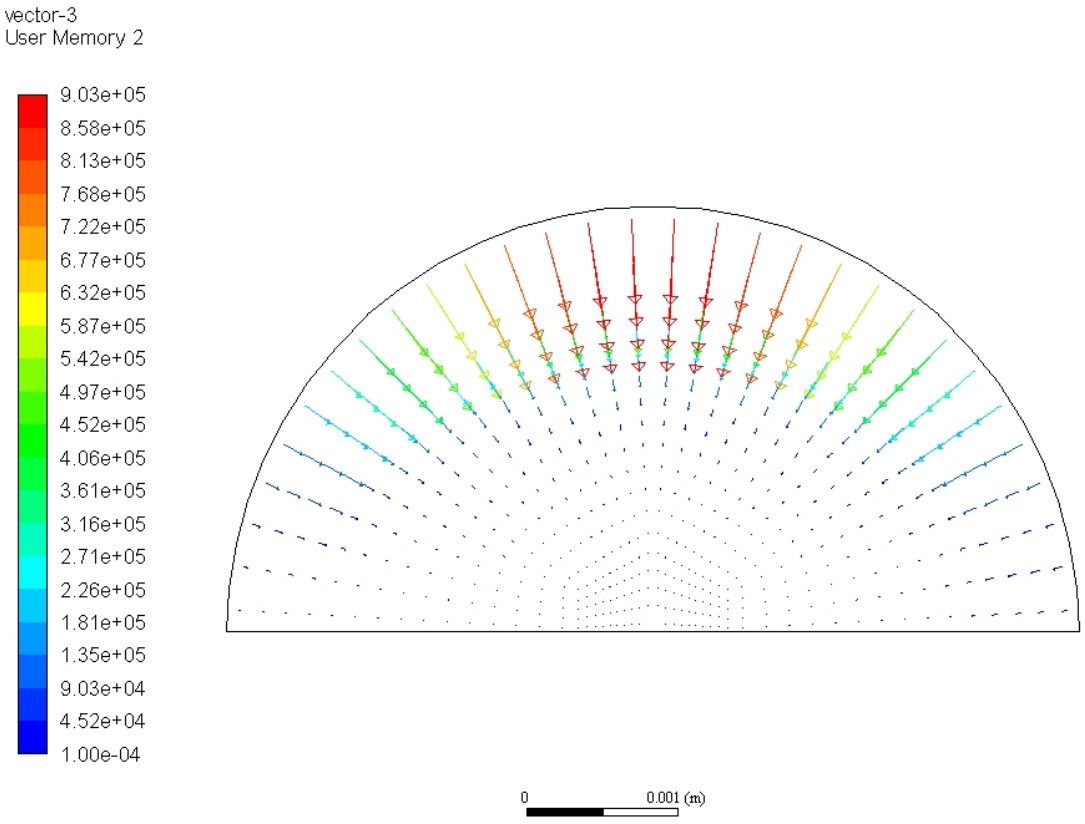

Figure 20: EML field applied to the germanium sample during heating.

shown in Figure 20 which results in the heater driven flow pattern in Figure 21. The model was run to assess both density models with Gruner's viscosity model; the resulting maximum flow velocities are given in Table 6 with the corresponding Reynolds numbers that describe the flow. The excessively high Reynolds numbers agree with the observations in the video that indicate the flow is very turbulent under these conditions.

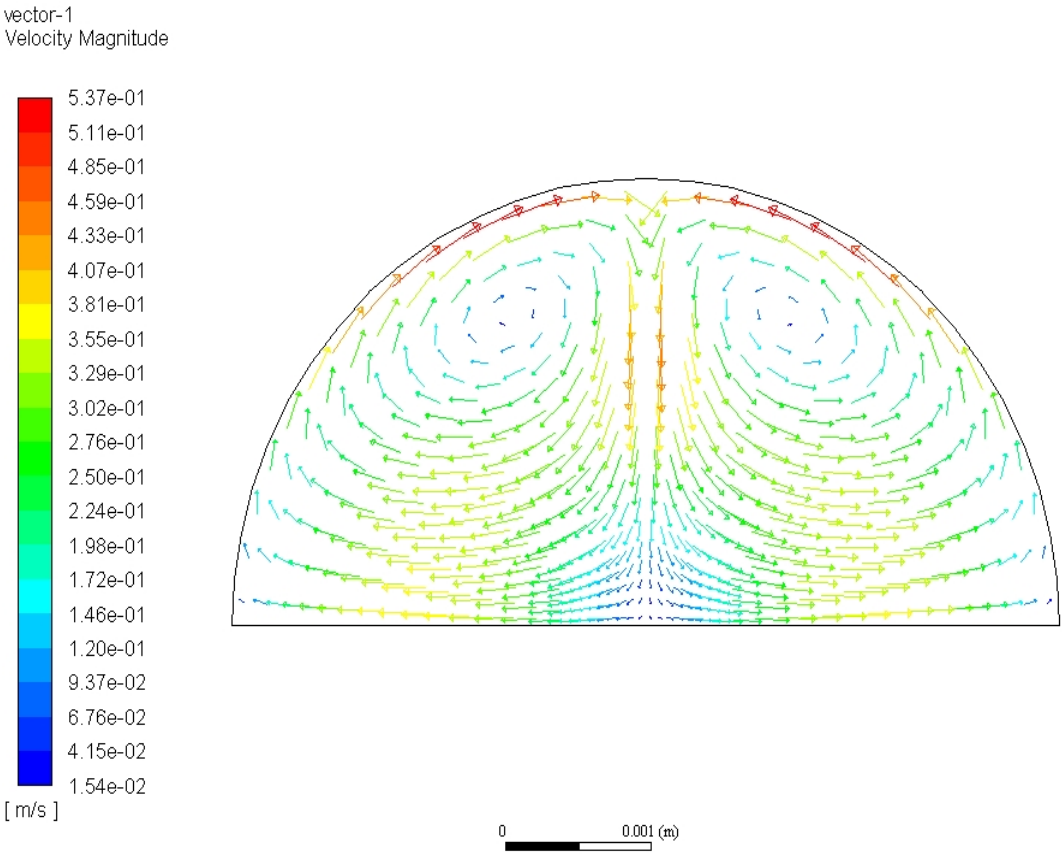

Figure 21: Heater-dominated flow within the germanium sample resulting from the applied EML field and high temperature liquid property conditions.

Table 6: Maximum velocities and Reynolds numbers calculated to describe the flow within the sample at the cycle high temperature using the applied EML field and the Gruner viscosity model.

	Maximum Flow Velocity (m/s)	Reynolds Number
Luo Density	0.657	69,400
Iida Density	0.623	72,700

The flow immediately prior to recalescence was also of interest to collaborators. During cooling the flow was driven by the positioner coils. The electromagnetic field during cooling is shown Figure 22. This field was applied to the property conditions expected at the recalescence temperature and the model simulated the positioner driven flow pattern given in Figure 23. The resulting maximum flow velocities and the corresponding Reynolds numbers for the different property models are shown in Table 7. The calculated Reynolds numbers provide strong indication in support of the video evidence that the flow in the drop prior to recalescence is highly turbulent.

Table 7: Maximum velocities and Reynolds numbers calculated to describe the flow within the sample under the reduced electromagnetic field and using Gruners viscosity model.

	Maximum Flow Velocity (m/s)	Reynolds Number
Luo Density	0.0658	6600
Iida Density	0.0663	6450

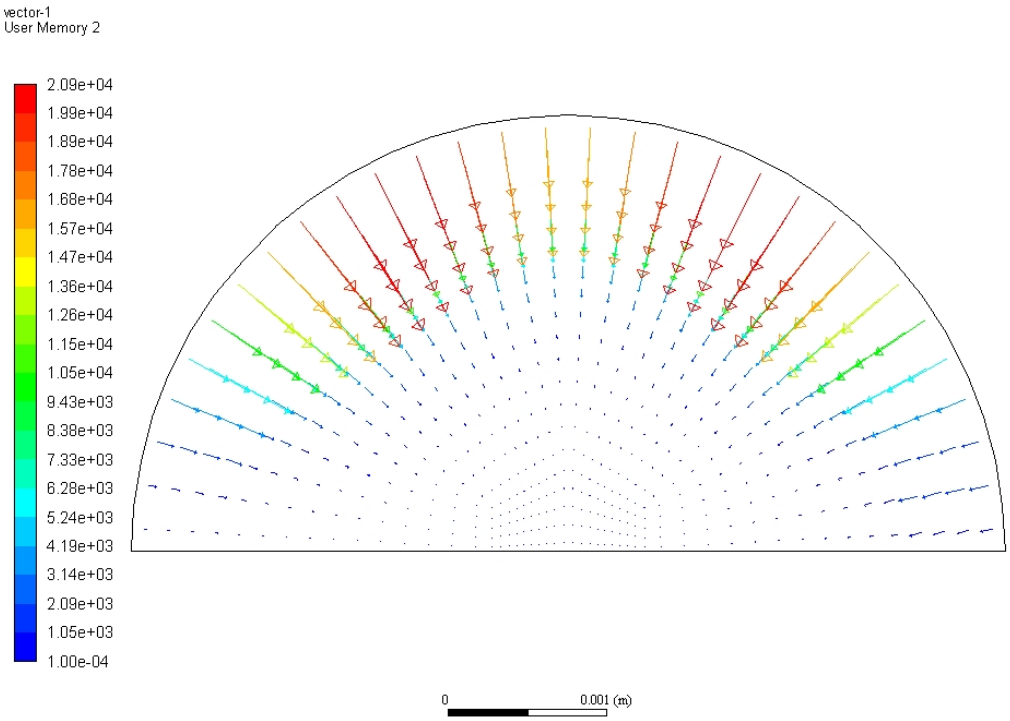

Figure 22: Applied electromagnetic field to the germanium sample during cooling.

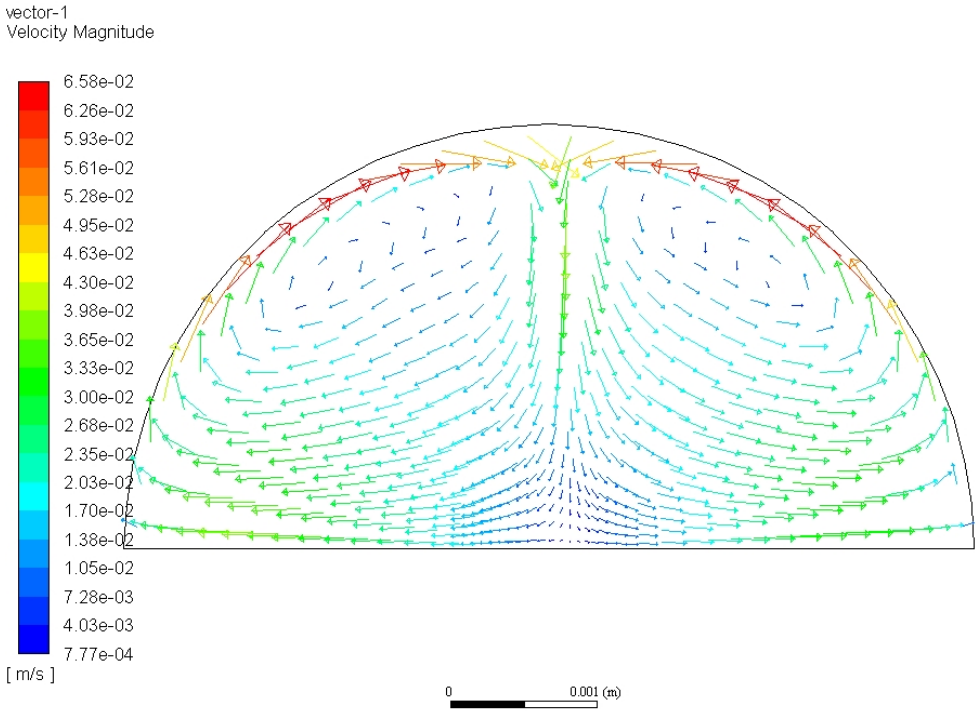

Figure 23: Fluid flow pattern calculated for the germanium sample immediately prior to recalescence using the turbulent flow model.

6.4 Conclusions

Based on both models for the flow within the droplet and video evidence, the flow within the droplet is highly turbulent in all conditions experienced in the EML experiment we analyzed. As the parabolic flight experiments usually use even higher positioning currents, the flow there was likely turbulent as well. Therefore, these experiments should account for the turbulence when interpreting the results, particularly of oscillation measurements.

CHAPTER 7

$TI_{39.5}\,ZR_{39.5}\,NI_{21}$

Current work is exploring solidification and the thermophysical properties of various Ti-Zr-Ni alloys [37] with special interest focusing on the formation of quasicrystal and glass formation [47]–[49]. For compositions near 21 at% nickel, a metastable quasicrystal structure forms during solidification instead of a more stable Laves phase [47]. Recent work by collaborators has explored the formation of quasicrystals as determined by the structure of the melt and have found correlations between the nucleation barrier and the presence of icosahedral short range order [47]. While several models for solidification in complex alloys are being explored, the coupled-flux nucleation model is of particular interest because it directly relates diffusive and interfacial flux of species in the melt [50], [51]. The coupled-flux nucleation model is discussed further in Chapter 2.3: Fluid Flow and Solidification Studies. However, further study of this models requires that solute gradients in the melt be controlled by diffusion and not shear in the melt.

Current work is using Ti-Zr-Ni as a case study for the coupled-flux nucleation model and requires the quantification of the internal flow within levitated drops. $Ti_{39.5}Zr_{39.5}Ni_{21}$ was processed in batch 2.1 of the ISS-EML campaign to study the solidification and the thermophysical properties of the melt [37]. The work presented here provides an analysis of the fluid velocity and shear rates in the melt near recalescence with additional details on the analyzed cycles available in [52]. The flow was modeled using the methods described in Chapter 3 to calculate the flow velocity, Reynolds number and shear-strain rate during cooling.

7.1 Material Properties

The $Ti_{39.5}Zr_{39.5}Ni_{21}$ sample processed in the ISS-EML facility is 6mm in diameter. This alloy was expected to have a liquidus at 1093K and achieve 150K undercooling [37].

Recent work in ESL was used to measure the density, conductivity, and viscosity of this alloy [53]. The conductivity of the melt was approximated to be 6.49 S/m over the temperature range of interest. During the work by the Kelton group [53], the density of the melt was measured and fit the following trend:

$$\rho = 6.1927 - 0.000287T \ (g/cm^3) \quad (17)$$

The recent viscosity measurements in ESL by the Kelton group [53] (KFK), have been compared to prior measurements and fits of the viscosity using an Arrhenius and VFT fit. The results are shown below in Figure 24, in which the KFK ESL measurements are plotted in blue, the Arrhenius fit to Bradshaw's data is given in orange, and the VFT fit to Bradshaw's data is plotted in grey. For the purposes of extrapolating the ESL data, the VFT fit to Bradshaw's measurements was used as is given in Equation 18 [54].

$$\mu = \mu_0 * exp\left(\frac{DT_0}{T - T_0}\right) = 0.00225 * \exp\left(\frac{1.88 * 686.25}{T - 686.25}\right) \quad (18)$$

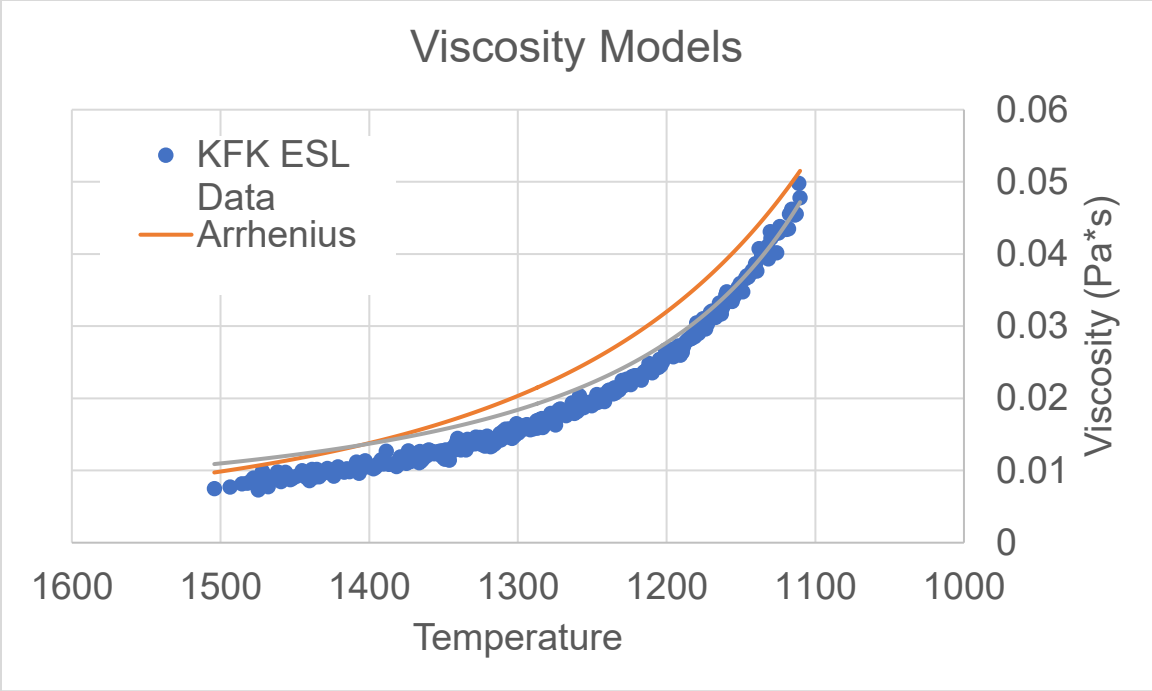

Figure 22: The KFK ESL viscosity measurements are plotted over the range of cooling with both Arrhenius and VFT fits as published by Bradshaw [54].

7.2 Model Results

Our collaborators requested 9 different experimental cycles be analyzed from the ISS-EML processing. From these 9 cycles, 6 unique models were run to analyze the flow during cooling through the recalescence. The processing conditions for each cooling cycle are given in Table 8. Cycles 49 and 50 were processed under identical experimental conditions and were therefore modeled as one cycle over an extended temperature range. This was also done with cycles 65 and 66, as well as cycles 55 and 62.

Table 8: Experimental parameters for the ISS-EML used to control the $Ti_{39.5}Zr_{39.5}Ni_{21}$ sample during the cooling phase of the cycles.

Cycle Number	Heater Voltage	Positioner Voltage	Heater Oscillating Amplitude	Positioner Oscillating Amplitude
Cycle 11	0.00	5.71	17.5	188.9
Cycle 49	0.00	3.87	17.5	137.1
Cycle 50	0.00	3.87	17.5	137.1
Cycle 64	0.00	3.99	17.5	140.5
Cycle 65	0.00	9.39	17.5	292.9
Cycle 66	0.00	9.39	17.5	292.9
Cycle 53	0.01	5.71	19.2	188.9
Cycle 55	0.00	5.71	17.5	188.9
Cycle 62	0.00	5.71	17.5	188.9

By evaluating the models with the EML force field conditions specified in Table 8 the flow parameters were calculated and the results for the cycles at the recalescence temperature are presented in Table 9. It can be seen in the table that all the cycles modeled where well below the laminar-turbulent transition. The Reynolds numbers are much less than 600, clearly indicating laminar flow [16]. In addition, the shear-strain rate at the recalescence temperature is also presented in Table 9.

Table 9: The summary of the calculated flow parameters near the recalescence temperature.

Cycle Number	Recalescence Temperature (K)	Maximum Velocity (m/s)	Reynolds Number	Shear-strain Rate
Cycle 11	990	0.00119	0.23	2.89
Cycle 49 and 50	980	0.00128	0.25	2.52
Cycle 64	1030	0.00242	0.89	4.87
Cycle 65 and 66	1020	0.00284	0.94	8.07
Cycle 53	1030	0.00263	0.97	6.15
Cycle 55 and 62	1020	0.00210	0.69	5.02

During cooling the flow was analyzed using the EML field to calculate the velocity and shear-strain rate in the drop. Figure 26 show the velocity on the left and the contours of the shear-strain rate in the drop as calculated for conditions immediately prior to recalescence in $Ti_{39.5}Zr_{39.5}Ni_{21}$ for cycle 11. Over the temperature range of interest, the flow was characterized by Reynolds numbers much less than the expected laminar-turbulent transition at 600 for all modeled cycles. The evolution of the flow in cycle 11 is shown in Figure 25 for Bradshaw's Arrhenius fit and VFT fit [54] and the viscosities measured in more recent work. This laminar flow behavior is consistent across all cycles of interest in this sample.

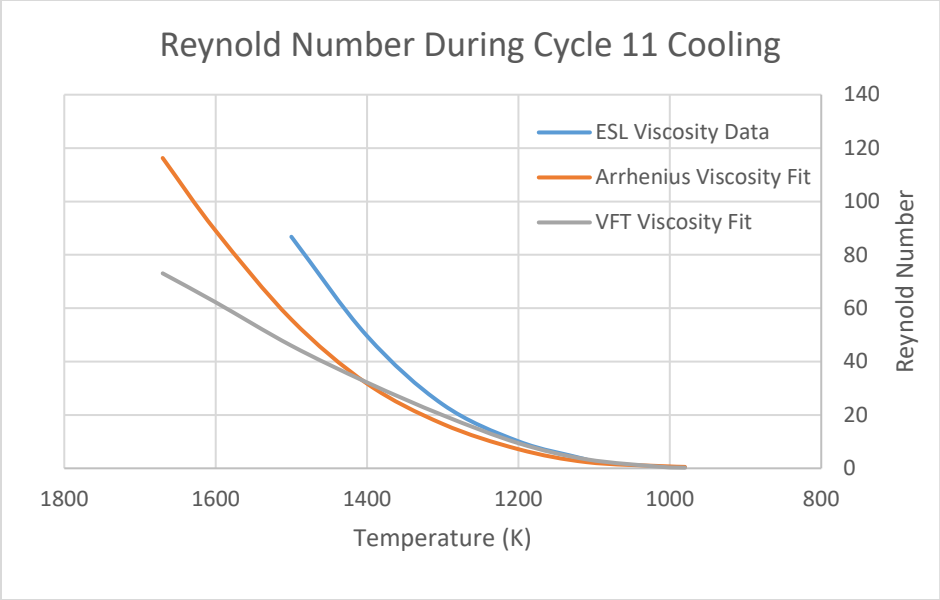

Figure 23: Reynolds numbers characterizing the flow during cooling in cycles 11 based on the maximum flow velocity using Bradshaw's Arrhenius fit, Bradshaw's VFT fit, and the KFK ESL measurements.

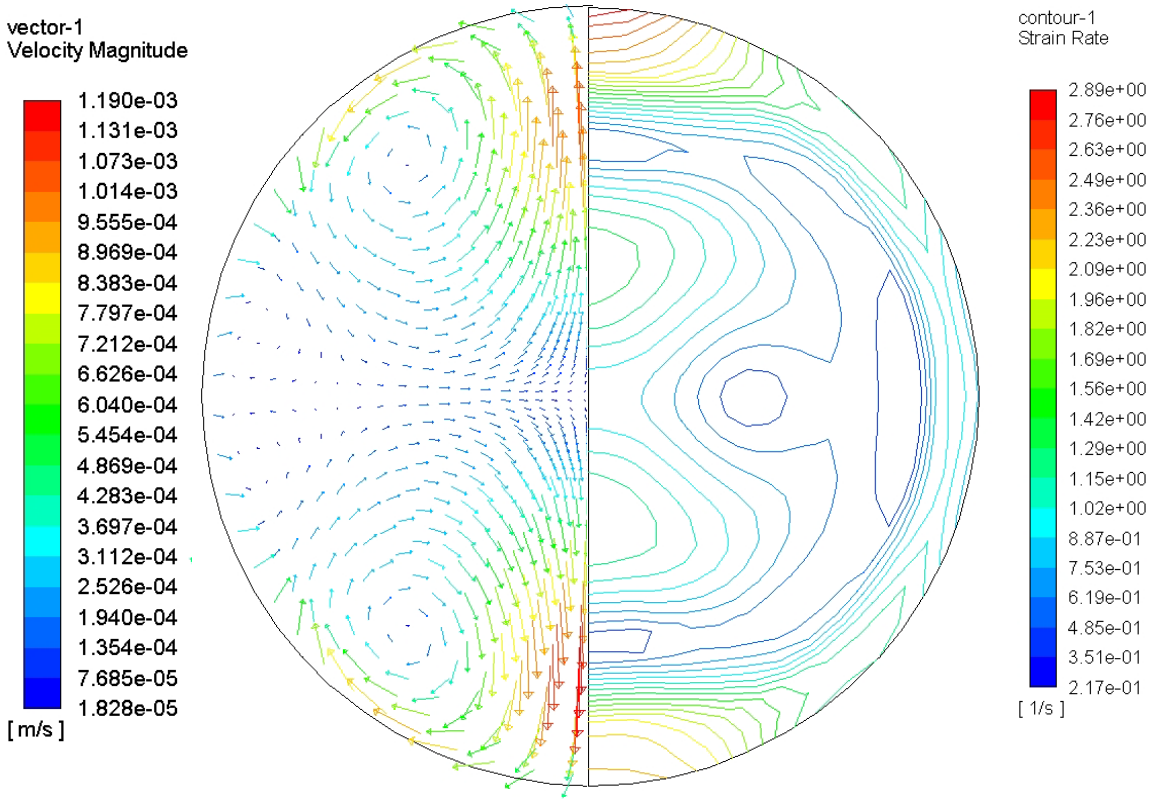

Figure 24: The fluid flow calculated using the cooling conditions during cycle 11 and modeled using the materials properties of $Ti_{39.5}Zr_{39.5}Ni_{21}$ at 980K. The velocity profile is shown on the left in which the maximum flow velocity is 1.190×10^{-3} m/s. The shear-strain rate contours are plotted on the right in which the peak strain rate is 2.9 s^{-1} near the poles of the sample; however, most of the sample is below 1.2 s^{-1}.

For the shear rate in the sample, science requirement document (SRD) specifies "Using an estimate of the critical cluster density for steady-state obtained from the coupled-flux modeling (§3.7), clusters will be separated by d = 1 μm – 0.1 μm, if uniformly spaced. For the cooling rate of approximately 10 °C/s, they should remain apart for at least t_d =1 s to avoid convective contamination in the evolution of the cluster distribution. The maximum allowed shear-strain rate to avoid collisions between the diffusion fields of the critical nuclei is $d/(t_d*2L)$, or 5 – 50 s^{-1}. These are upper limits, given the uncertainties in the assumptions inherent in this estimate. Further, cluster evolution is governed not only

by the critical size clusters, but by the entire cluster population, leading to a much smaller estimate on the cluster separation. A rate that is two orders of magnitude less (0.05 – 0.5 s^{-1}) than the above estimate, is, therefore, deemed necessary to assure a diffusion-controlled experiment." [55]. These parameters were determined for $Ti_{39.5}Zr_{39.5}Ni_{21}$ by Kelton, however, the actual experimental cooling rates varied from the prescribed 10 °C/s and are given below in Table 10.

Table 10: Cooling rates for $Ti_{39.5}Zr_{39.5}Ni_{21}$ prior to recalescence and solidification

Cycle Number	Recalescence Temperature (K)	Shear-strain Rate (s^{-1})	Cooling Rate Prior to Recalescence (K/s)
Cycle 11	990	2.89	-2.38
Cycle 49	980	2.52	-3.02
Cycle 50	980	2.52	-3.02
Cycle 64	1030	4.87	-30.88
Cycle 65	1020	8.07	-27.75
Cycle 66	1020	8.07	-25.48
Cycle 53	1030	6.15	-2.18
Cycle 55	1020	5.02	-7.95
Cycle 62	1020	5.02	-4.43

While the shear-strain rates in the cycles are within the calculated target range for cooling rates near 10 °C/s, although not the broader range intended to account for the subcritical clusters. Additionally, the cycles did not cool at the assumed rate. Cycles 64-66 cooled between approximately 2.5 and 3 times faster than was assumed. As a result, the

shear-strain rate target needs to be recalculated for these cycles using the larger cooling rate. The Kelton group is currently working on these updated calculations.

In the other analyzed cycles, the shear-strain rate was within the required shear-strain rate based on the nominal calculation but not in the broader range to account for the subcritical clusters. However, the cooling rate was significantly lower than the assumed target. These cycles should also have the shear-strain rate targets reassessed based on the cooling rates achieved in the experiment to ensure that diffusion controlled the effects seen during the experiment.

7.3 Conclusions

During cooling, the $Ti_{39.5}Zr_{39.5}Ni_{21}$ sample is calculated to have laminar flow in all cycles analyzed over the full range of cooling conditions. The shear rates were also determined to be within the nominal specifications for the specified cooling rates, although not within the broader specifications to account for any effects due to subcritical nuclei. However, the variation in the achieved cooling rates from the specifications given in the SRD may have changed the requirements for the shear-strain rate in the sample at recalescence. Calculations should be done for the different cooling rates reassess the targeted shear-strain rate and ensure the concentration profiles around subcritical nuclei did not interact.

CHAPTER 8

$CU_{50}ZR_{50}$

The $Cu_{50}Zr_{50}$ alloy was chosen to be used in ISS-EML solidification studies for its behavior in which the melt solidifies through dendrite growth congruently (without constitutional supercooling) [56] making it a useful model to investigate the effects of the redistribution of heat along the solidification front and the atomic attachment kinetics at the interface [57] in the absence of a solutal boundary layer. As described for the prior systems, models were analyzed in ANSYS Fluent to calculate and quantify the internal flow prior to recalescence in a molten $Cu_{50}Zr_{50}$ alloy processed in Batch 2 of the ISS-EML experiments. This sample was processed to take systematic measurements of the growth velocity as a function of the undercooling and to measure the thermophysical properties necessary to correlate synchrotron structural data and investigate liquid fragility and chemical ordering [37], [58].

There are 2 cycles of interest to our collaborators, cycle 28 and 29, which were defined by the same cooling parameters and were therefore modeled together. During the cooling phase of the cycle the control voltage applied to the amplifier for the heater was 0.000 V which results an oscillating current of 17.5 A and the control voltage applied to the amplifier for the positioner was 3.879 V which results in 137.4 A applied by the oscillating current. The EML force field during processing is given in Figure 27.

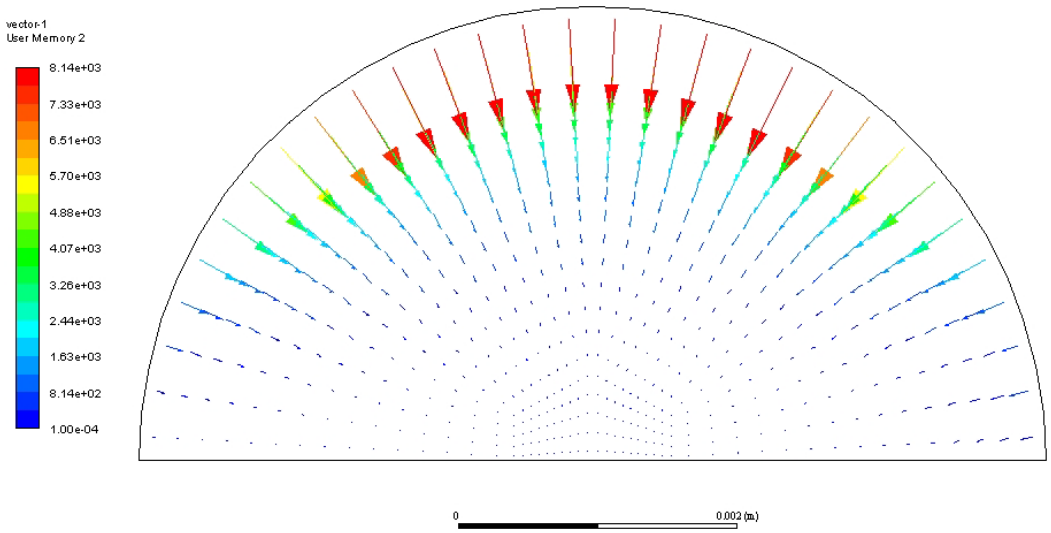

Figure 25: Electromagnetic force field calculated for cooling conditions of $Cu_{50}Zr_{50}$ in the ISS-EML facility. The conductivity of the melt is approximated to be 7.05×10^5 S/m. The amperage applied by the oscillating heater current is 17.5A and the amperage applied by the oscillating positioner current is 137.4A.

8.1 Material Properties

The models use the properties of $Cu_{50}Zr_{50}$ based on the measurement taken in recent work [59]. The electrical resistivity of the melt is estimated to be 1.4184 micro Ohm m which corresponds to a conductivity of 7.05×10^5 S/m over the temperature range of interest. The density and viscosity were measured in recent work [53], [59] and the VFT fit was applied to the viscosity data, resulting in the constants in *Table 11*.

$$\rho(T) = 7635.6 - 0.491T \ (kg/m^3)$$

19

$$\mu = \mu_0 * exp\left(\frac{DT_0}{T - T_0}\right)$$

20

Table 11: VFT fit constants for Cu50Zr50

Constants	Fitted Value
μ_0	0.001038
T_0	744.424
D	1.983

8.2 Model Results

Laminar flow models were analyzed with the properties of the melt to determine the behavior of the flow as the droplet cooled. The fluid flow pattern for this system is shown in the left hemisphere of Figure 28 and the shear-strain rate contour plots are given in the right hemisphere of Figure 28 with the results at the recalescence temperature of each cycle given in *Table 12*. In velocity profile, the flow is driven into the drop along the equator and returns to the surface of the drop at the poles where the force field is lower.

In both cycles of interest, the flow was slow and characterized by low Reynolds numbers during the entire cooling phase of the cycle. The results are plotted in Figure 29, where Reynolds numbers for the flow are much less than the expected laminar-turbulent transition of 600 [16]. The evolution of the maximum shear-strain rate in the drop during cooling is also plotted in Figure 6.

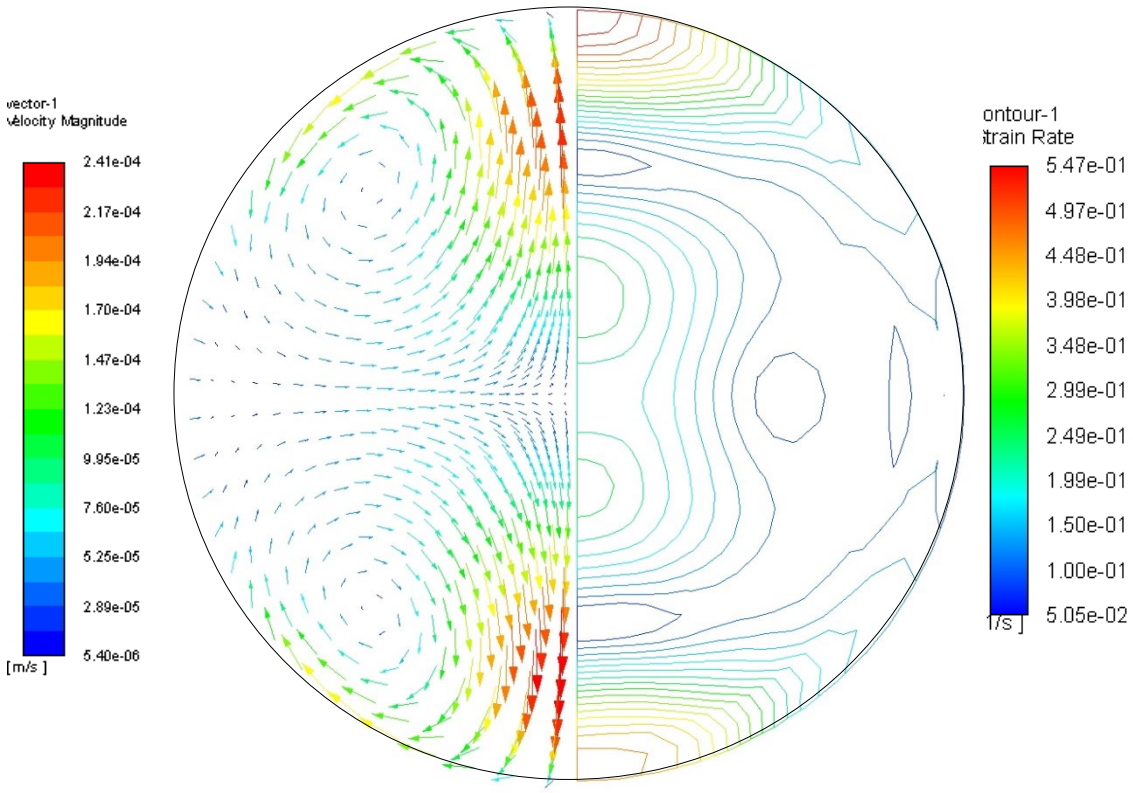

Figure 26: The flow calculated for $Cu_{50}Zr_{50}$ in the ISS-EML experiments immediately prior to recalescence at 950 K. The left hemisphere shows the velocity field in which the maximum flow velocity is 2.407×10^{-4} m/s. On the right side, the shear-strain rate contours are plotted for these flow conditions. The maximum shear-strain rate is 0.547 s^{-1} with most of the sample below 0.25 s^{-1}.

The shear-strain rate is largest near the poles of the sample and is approximately 6x larger than the shear-strain rate along the equator of the sample, as is shown in Figure28. The maximum shear rate in both cycles is below the shear-strain rate requirements calculated for $Ti_{39.5}Zr_{39.5}Ni_{21}$ cooled at 10°C [37], [55]. However, both cycle 28 and cycle 29 of the $Cu_{50}Zr_{50}$ sample had a cooling rates that were almost an order of magnitude slower, given in *Table 12*. Additionally, the differences in composition of the melt may change the chemical and thermodynamic driving forces for nucleation. The shear-strain

rate target for the $Cu_{50}Zr_{50}$ sample should be reviewed and recalculated if necessary, to ensure that the solidification experiment was diffusion controlled and that the phase field of the nuclei clusters did not overlap.

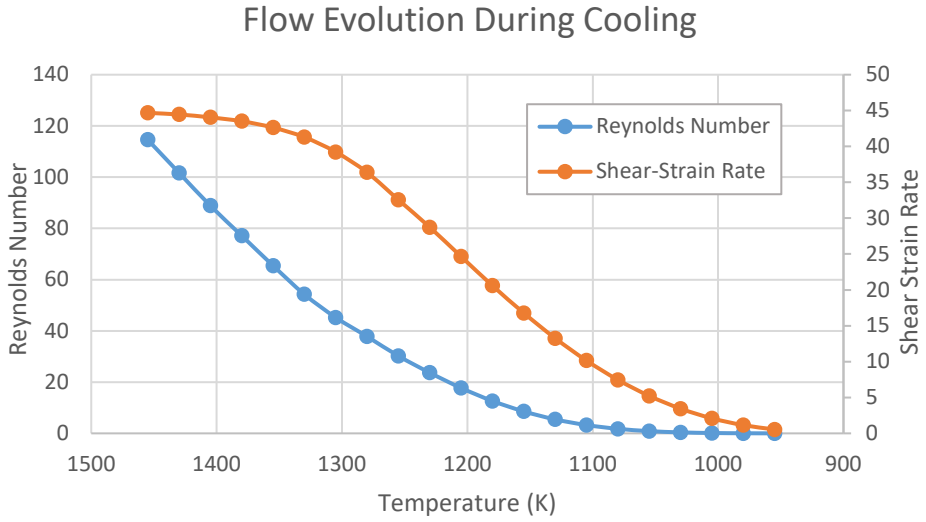

Figure 27: Evolution of flow in $Cu_{50}Zr_{50}$ during cooling in ISS-EML experiments.

Table 12: Flow simulation results for $Cu_{50}Zr_{50}$ cycles

	Cycle 28	Cycle 29
Recalescence Temperature (K)	955	965
Cooling Rate Prior to Recalescence (°C/s)	-1.46	-1.71
Viscosity (Pa s)	1.149	0.837
Maximum Flow Velocity (m/s)	2.407	3.308
Reynolds Number	0.0098	0.0184
Shear-Strain Rate (s^{-1})	0.5469	0.7515

8.3 Conclusions

Computational fluid dynamics models were analyzed to characterize the flow and shear-strain behavior in electromagnetic-levitation experiments on $Cu_{50}Zr_{50}$ in the ISS-EML facility. During the entire range of the cooling phase of the experiment, the Reynolds number characterizing the flow was well below the known laminar-turbulent transition, which indicates the flow to be laminar and slow. Additionally, the shear-strain rate was calculated during the cooling phase of the sample. As the sample cooled, the maximum shear-strain rate in the sample decreased. At the time of recalescence, the shear-strain rate was within the specifications given in the Science Requirement Document for $Ti_{39.5}Zr_{39.5}Ni_{21}$ (which has been used as a basis of comparison since no target rates were given for $Cu_{50}Zr_{50}$); however, the $Cu_{50}Zr_{50}$ sample had cooled at a significantly slower rate than was in the specifications for the $Ti_{39.5}Zr_{39.5}Ni_{21}$ sample. In evaluating the strain rate in this sample against the coupled-flux model for nucleation, calculations should be done for $Cu_{50}Zr_{50}$ at this lower cooling rate to reassess the targeted shear-strain rate and ensure the concentration profiles around subcritical nuclei did not interact during the experiment.

CHAPTER 9

VITRELOY 106

Amorphous metals, or bulk metallic glasses, have been developed to provide high tensile strength and high corrosion resistance by preventing the formation of grain boundaries [60]. Vitreloy was an early metallic glass that resists crystallization in the undercooled liquid state, developed by Prof. W.L. Johnson at Caltech and is licensed to the LiquidMetal corporation [61], [62]. Since its development, Vitreloy 106 has been widely-studied as a beryllium-free bulk metallic glass; however, measurements on the thermophysical properties of the melt have only recently been performed using containerless processing techniques [63].

A Vit106 ($Zr_{57}Cu_{15.4}Ni_{12.6}Al_{10}Nb_5$) sample was processed during batch 1.2 of the ISS-EML campaign in which the sample was processed to study the nucleation kinetics, solidification velocity, thermophysical properties, and behavior of the undercooled melt [64]. The work presented here provides an analysis of the fluid velocity and shear rates in the melt near recalescence; additional details on the analyzed cycles are available in [65], as reported to collaborators. The flow was modeled using the methods described in Chapter 3 to calculate the flow velocity, Reynolds number and shear-strain rate during cooling.

9.1 Material Properties

The models use the properties of Vit106 based on recent measurements work [59], [66]. The electrical resistivity of the melt is estimated to be 1.667 micro-Ohm-m, which corresponds to a conductivity of 6.00×10^5 S /m over the temperature range of interest. The density and viscosity were measured in recent work [66], [67].

$$\rho(T) = 6816.5 - 0.335T\ (kg/m^3)$$

21

The data was fit to both a VFT and KKZNT fit. At low temperatures, the VFT viscosity gets very large and the simulations are no longer stable. The form of the VFT fit is given below and the constants are provided in Table 13.

$$\mu = \mu_0 * exp\left(\frac{DT_0}{T - T_0}\right)$$

22

Table 13: VFT Constants for Vit106

Constants	Fitted Value
μ_0	0.001171 Pa·s
T_0	745.090 K
D	2.501

At low temperatures, the KKZNT fit [67] was used. However, per the request of our collaborators who have developed the related theory the KKZNT was not used at temperatures above T*. While the KKZNT is not applicable at temperatures above T^*, over the range of the experiments the differences are small. The form of the KKZNT fit is given below and the constants are provided in Table 14.

$$\mu = \mu_0 * exp\left(\frac{E_\infty + T^* B\left[\frac{T^* - T}{T^*}\right]^Z \Theta(T^* - T)}{T}\right)$$

23

Table 14: KKZNT Constants

Constants	Fitted Value
μ_0	0.001231 Pa·s
E_∞	3833.27 J/mol
T^*	1471.70 K
B	12.27
Z	1.701

The viscosity models are plotted over the temperature range of interest with the measurements in Figure 30. It can be seen that the viscosity modeled by the KKZNT fit is always less than the viscosity modeled by the VFT fit. The following results use the KKZNT fit to relate the viscosity to the temperature of the sample in the simulations and as a result, the following results are the upper bound of the velocity and shear rate during the experiments.

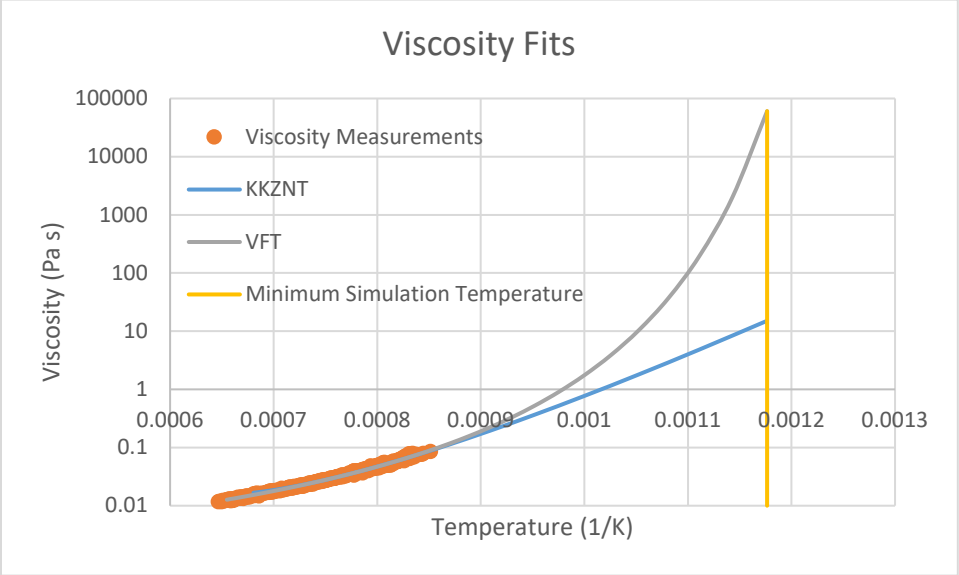

Figure 28: Viscosity fits plotted as a function of 1/T, such that high temperatures are on the left, and extended over the temperature range of interest.

9.2 Model Results

Using the properties of the liquid alloy, fluid flow simulations were run with laminar flow models to predict the correlation of the fluid flow with the properties of the flow as the droplet cooled. The electromagnetic field are the forces that drive the flow patterns.

Table 15: Summary of flow simulation results for cycles of interest in Vit106

	Cycle 1	Cycle 8	Cycle 60	Cycle 68
Recalescence Temperature (K)	850	850	875	855
Cooling Rate Prior to Recalescence (°C/s)	1.41	0.85	6.06	19.63
Viscosity (Pa s)	15.1	15.1	8.37	13.4
Maximum Flow Velocity (m/s)	1.64×10^{-5}	1.89×10^{-5}	1.45×10^{-4}	2.05×10^{-5}
Reynolds Number	4.61×10^{-5}	5.32×10^{-5}	7.36×10^{-4}	6.51×10^{-5}
Maximum Shear-Strain Rate (s^{-1})	0.032	0.047	0.257	0.049

The flow was calculated and analyzed over the full temperature range of the relevant cycles and was found to be characterized by Reynolds numbers much less than the 600 that characterizes the laminar-turbulent transition. The evolution of the parameters used to characterize the flow during cooling is plotted in Figure 31 where it can be seen that the Reynolds number and shear-strain decreases with decreasing temperature. The flow is shown in the drop in Figure 32 in which the velocity field and shear-strain rate are shown for cycles 60, which is representative of all four cycles analyzed for Vitreloy 106.

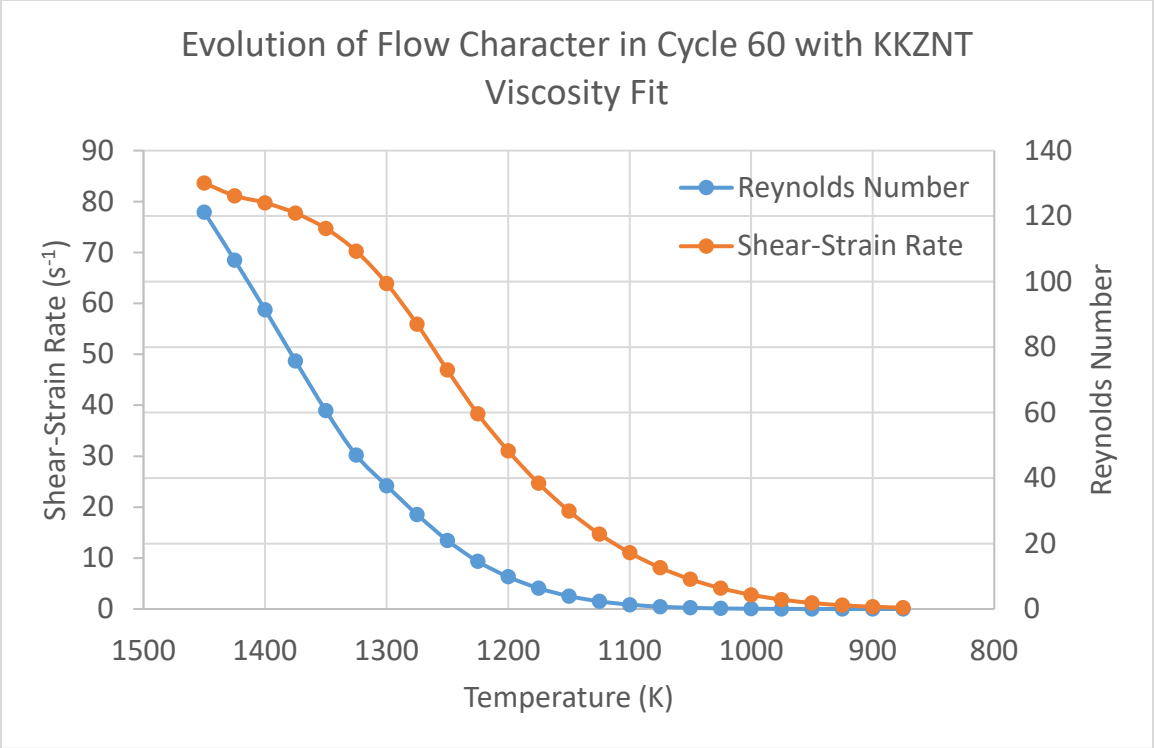

Figure 29: Evolution of flow metrics in Vit106 experiments in ISS-EML using the KKZNT viscosity fit over the cooling range of cycle 60.

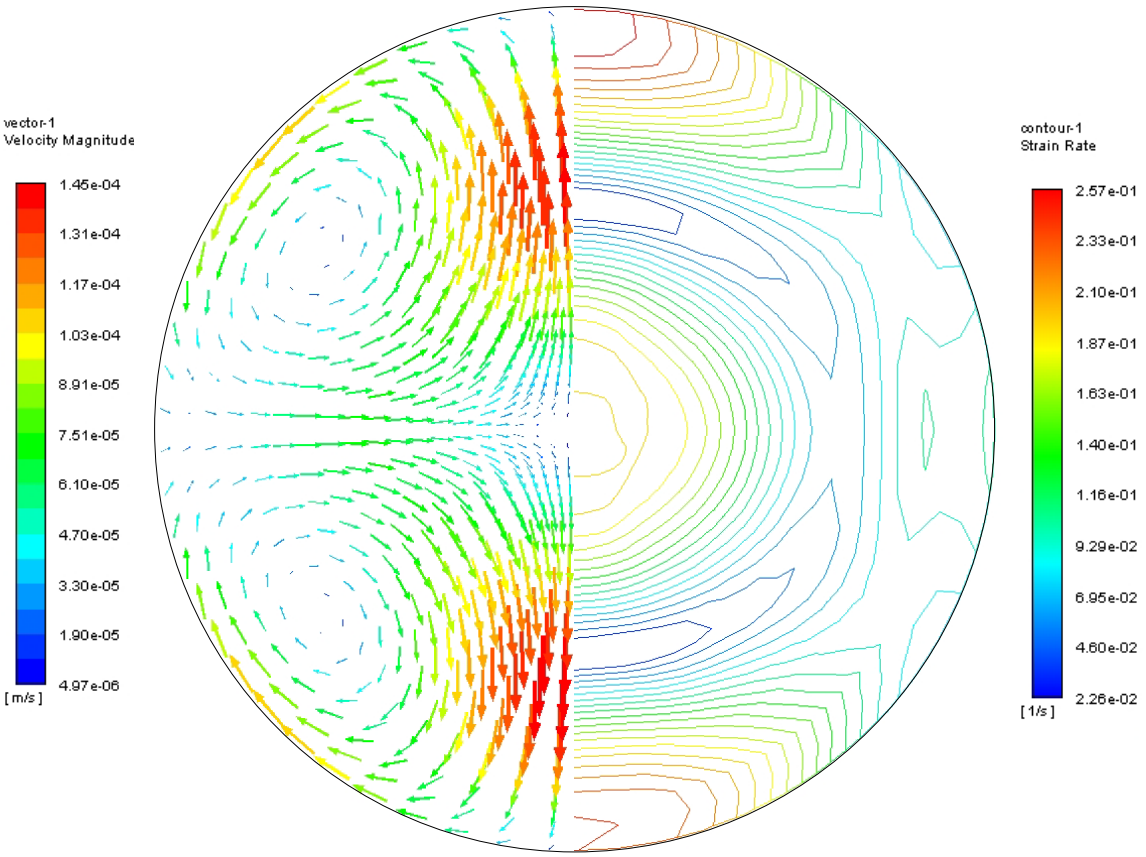

Figure 30: Flow calculated for the recalescence conditions during cycle 60 of the ISS-EML experiments on Vit106. On the left the velocity field is shown in which the maximum flow velocity is 1.45×10^{-5} m/s which gives a Reynolds number of 7.36×10^{-4}. The shear-strain rate contour is shown on the right in which maximum shear-strain rate is 0.257 s^{-1} with most of the sample below 0.187 s^{-1}.

9.3 Conclusions

Computational fluid dynamics models were analyzed to characterize the flow and shear-strain behavior in electromagnetic-levitation experiments on Vit106 in the ISS-EML facility. During the entire range of the cooling phase of the experiment, the Reynolds number characterizing the flow was well below the known laminar-turbulent transition, which indicates the flow to be laminar and slow. Additionally, the shear-strain

rate was calculated during the cooling phase of the sample. As the sample cooled, the maximum shear-strain rate in the sample decreased. At the time of recalescence, the shear-strain rate was within the specifications given in the Science Requirement Document for $Ti_{39.5}Zr_{39.5}Ni_{21}$; however, shear rates for the Vit106 sample were not specified in the SRD. Also, the Vit106 sample had cooled at a different cooling rates than were specified for $Ti_{39.5}Zr_{39.5}Ni_{21}$. Calculations of the nucleation rates should be done for Vit106 at this lower cooling rate to reassess the targeted shear-strain rate and ensure the concentration profiles around subcritical nuclei did not interact during the experiment.

CHAPTER 10

$ZR_{64}NI_{36}$

In addition to complex alloys like Vit106, there are number of binary and ternary alloy that form metallic glasses under rapid solidification. This $Zr_{64}Ni_{36}$ alloy is well-studied as a binary analog system for multicomponent bulk metallic glass alloys. This binary alloy exhibits similar properties and solidification behavior to the bulk metallic glass alloys, while reducing the number of interacting species which simplifies the theoretical treatment of nucleation and solidification. This alloy is being used as a case study to understand the structure of metallic liquids in contactless levitation facilities [68].

This $Zr_{64}Ni_{36}$ alloy that was processed as part of batch 2 in the ISS-EML experiments seeking to discern a relationship between the undercooling and stirring rate. Further, measurements have been taken on the surface tension, viscosity, specific heat of the liquid, thermal transport, and electrical resistivity of the stable undercooled liquid to support ground-based synchrotron and neutron structural studies [37], [58]. Using the models described in chapter 3 a series of 5 cycles were analyzed to calculate the internal flow behavior; additional details on the analyzed cycles were reported in [69].

10.1 Material Properties

The models use the properties of $Zr_{64}Ni_{36}$ based on the measurements taken in recent work and provided through private communication with the researchers [53], [59]. The electrical conductivity of the melt is estimated to be 7.271×10^5 S /m over the temperature range of interest. The density and viscosity were measured in recent work [53], [59].

$$\rho(T) = 7301.2 - 0.334T \ (kg/m^3)$$

The data was fit to a VFT fit. The form of the VFT fit is given below and the constants are provided in Table 16 and is plotted over the measured viscosity values from the KFK ESL measurements [53] in Figure 33.

$$\mu = \mu_0 * exp\left(\frac{DT_0}{T - T_0}\right) \quad 25$$

Table 16: VFT fit constants for $Zr_{64}Ni_{36}$

Constants	Fitted Value
μ_0	0.001252 Pa·s
T_0	697.1651 K
D	2.5592

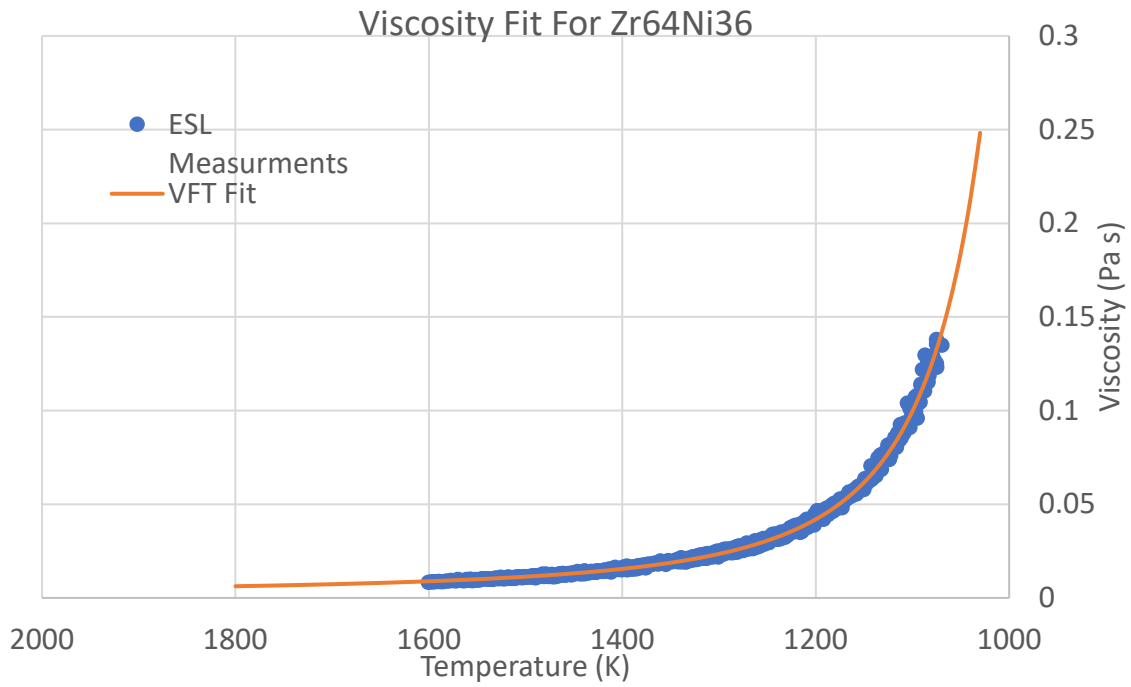

Figure 31: VFT viscosity fit plotted over the viscosity measurements and extended over the full temperature range of interest.

10.2 Model Results

As before, CFD simulations were run using the melt properties and laminar flow models to predict the correlation of the fluid flow with the properties of the flow as the droplet cooled. In the cycles of interest to our collaborators, several different EML melt cycles were analyzed with different EML force fields. The summary of the results for the analyzed cycles at their recalescence temperature are presented in Table 17.

Table 17: Summary of flow simulation results for cycles of interest in $Zr_{64}Ni_{36}$

	Cycle 19 And Cycle 22	Cycle 23	Cycle 26	Cycle 29
Recalescence Temperature (K)	1040	1050	1120	1110
Cooling Rate Prior to Recalescence (°C/s)	0.67 0.62	0.02	0.06	1.33
Viscosity (Pa s)	0.213	0.184	0.081	0.090
Maximum Flow Velocity (m/s)	$4.54x10^{-3}$	$5.24x10^{-3}$	0.038	0.074
Reynolds Number	1.19	1.58	25.7	45.8
Maximum Shear-Strain Rate (s^{-1})	8.2	9.5	70	130

The Reynolds numbers and shear-strain rates describing the flows are plotted in Figure 34 and the contour plot of the shear-strain rate that results from conditions at recalescence is given in Figure 35. Over the full cooling range, cycle 19, 22, and 23 the

Reynolds numbers calculated for the flow characterize the flow to be laminar over the full temperature range, based on the established laminar-turbulent transition [16]. In Figure 34, there is a clear shift in the rate at which the shear-strain rate changes during cooling. This shift is explained by a corresponding change in the rate of the flow during cooling. Near the recalescence temperature, the shear-strain rate is largest at the poles of the sample, as is given in Figure 35; however, at higher temperatures the shear-strain rate is largest at the equator of the sample.

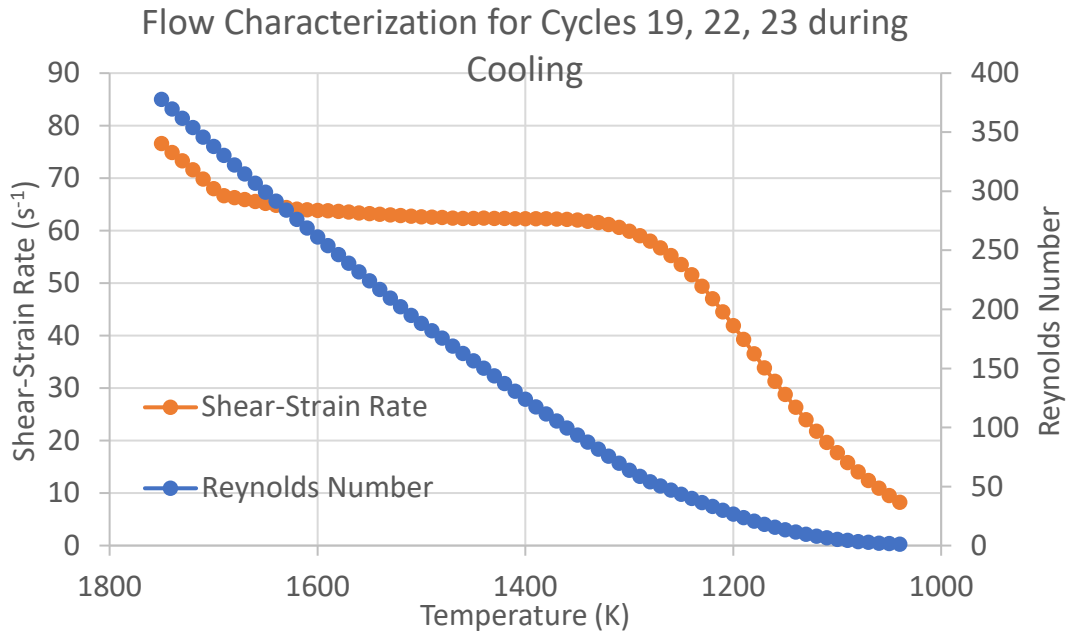

Figure 32: Evolution of flow metrics in $Zr_{64}Ni_{36}$ experiments in ISS-EML using the VFT viscosity fit over the cooling range of cycles 19, 22, and 23.

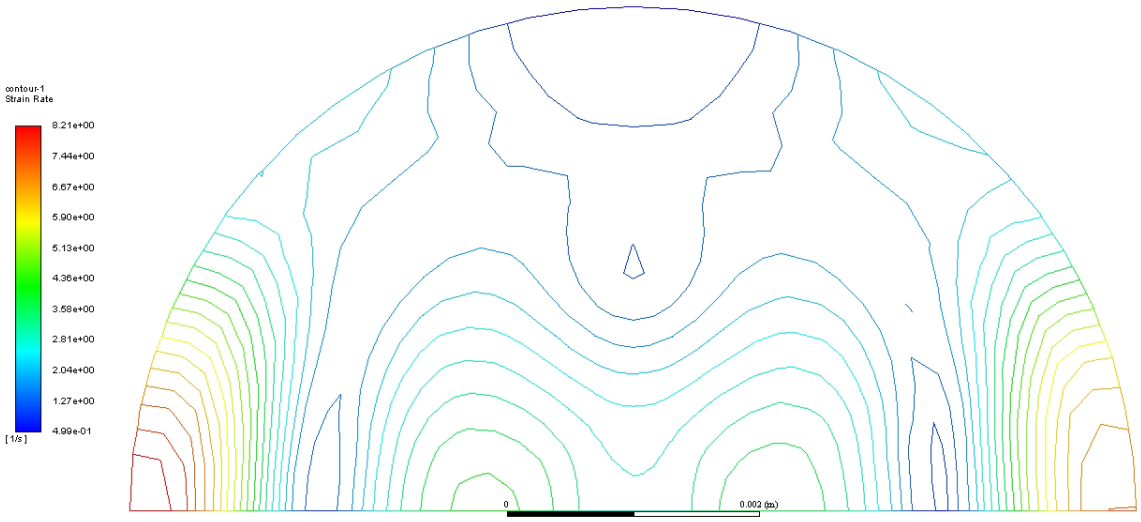

Figure 33: Contours for the shear-strain rate in $Zr_{64}Ni_{36}$ immediately prior to recalescence at 1040 K during the ISS-EML experiments for cycle 19 and cycle 22. The maximum shear-strain rate is 8.21 s^{-1} which results from a viscosity of 0.213 Pa s.

Just before recalescence, the sample's shear-strain rate is largest near the poles of the sample and is approximately 16x larger than the shear-strain rate along the equator of the sample, as is given in Figure 35. The maximum shear-strain rate in the sample near the recalescence temperature is higher than the shear-strain requirements calculated for $Ti_{39.5}Zr_{39.5}Ni_{21}$ cooled at 10°C/s [55]. Furthermore, the cycles for $Zr_{64}Ni_{36}$ cooled at rates that were more than an order of magnitude slower, given in Table 17, than was given in the specification. Additionally, the differences in the melt composition may change the chemical and thermodynamic driving forces for nucleation.

In cycles 26 and 29, the applied current was increased resulting in increased velocities and shear rates during processing. In cycles 29, the EML force field was large enough to drive flow that is characterized as turbulent based on the calculated Reynolds numbers. The Reynolds number is plotted over the full temperature range using both laminar and

turbulent models in Figure 36 where it can be seen that the flow crosses the laminar-turbulent transition during the cooling phase of the cycle. At 1350K, the laminar model predicts the flow crosses into the transitional region at Reynolds number of 600 [70]. Above 1350K for this cycle, the flow can be characterized as turbulent and the RNG k-ε model should be used to predict the flow.

The shear-strain rate calculated for the flow using both the laminar and turbulent flow models is given over the full range of interest for the cycle in Figure 37 where the shift in the shear-strain rate is shown in both models. It should be noted that in the shear-strain rate plot, the change in slope is due to the gradient of the shear-strain rate being largest at the equator of the drop at high temperatures and shifts to be greatest at the poles as the sample cools.

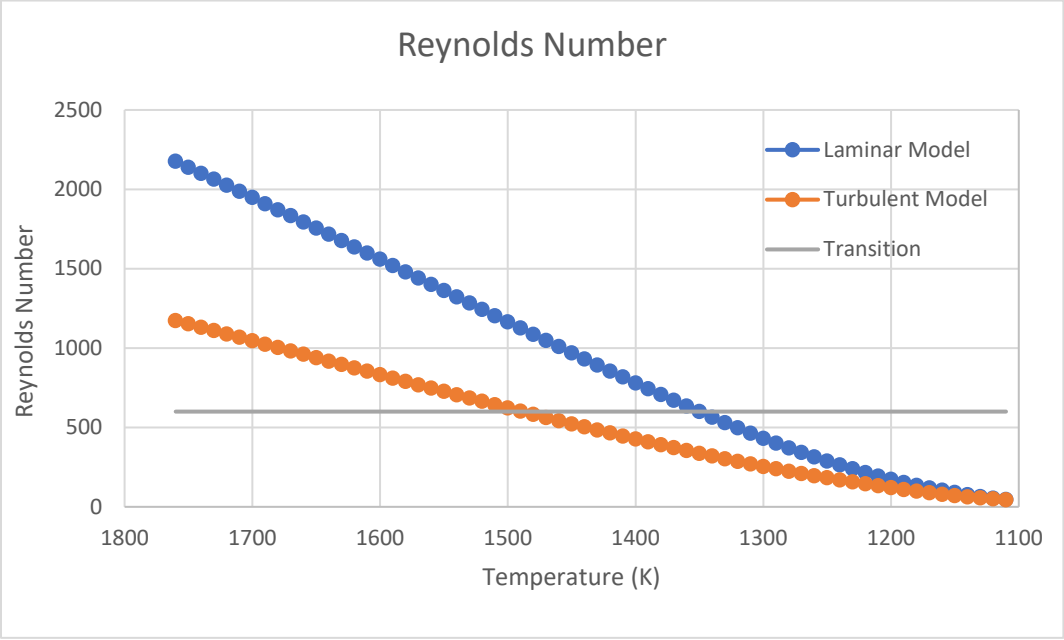

Figure 34: Evolution of Reynolds number in $Zr_{64}Ni_{36}$ during experiments in ISS-EML using the VFT viscosity fit over the cooling range of cycle 29. The oscillating heater current is 55.7 A and the oscillating positioner current is 191.7 A.

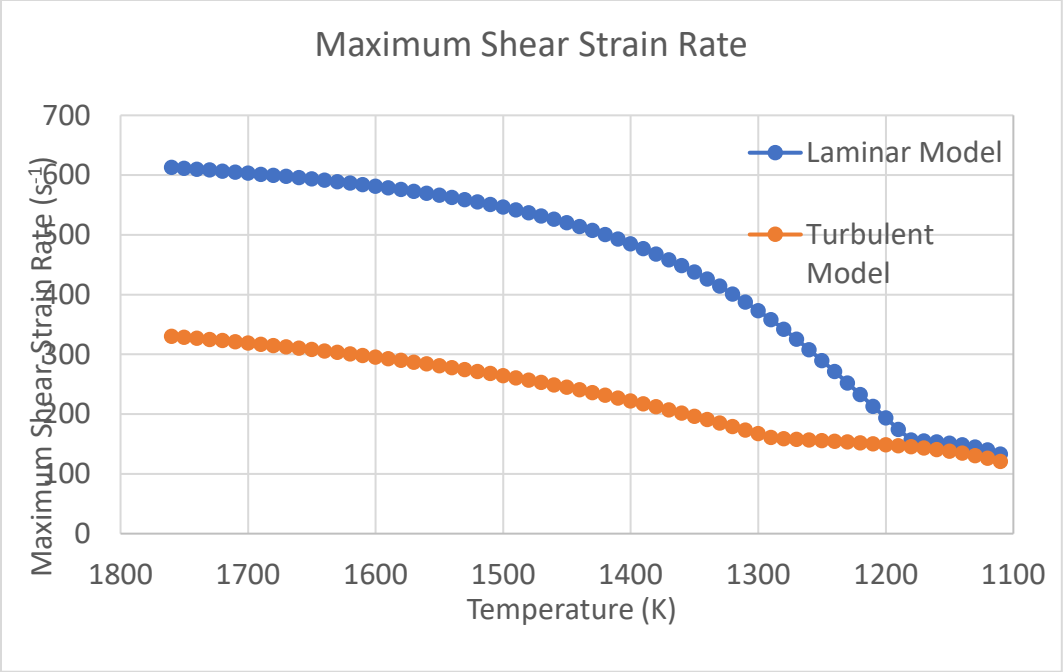

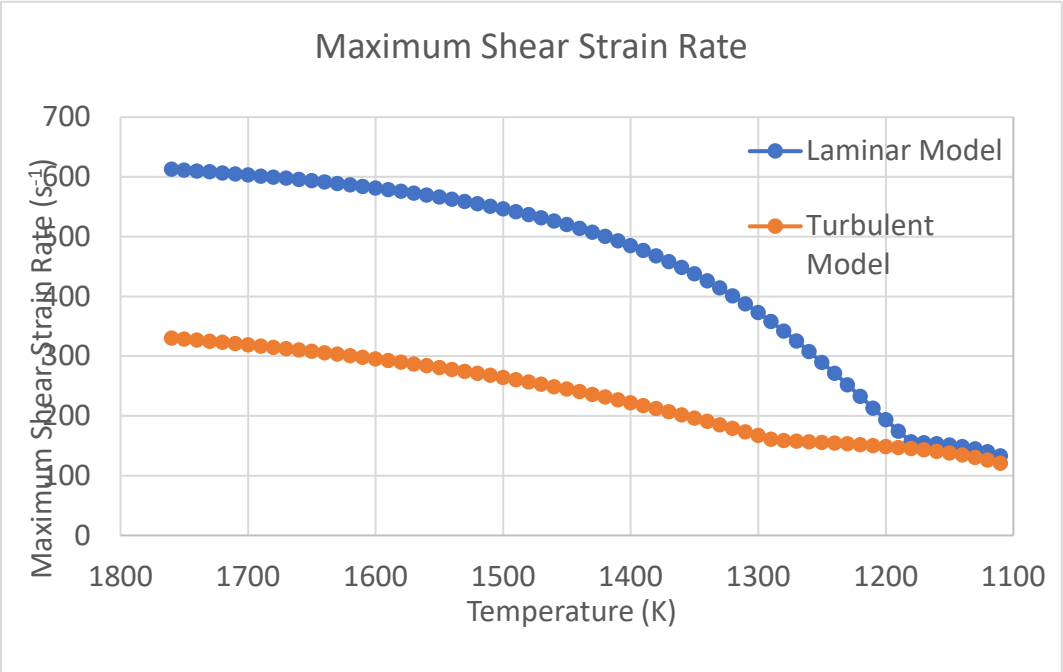

Figure 35: Evolution of the maximum shear-strain rate in $Zr_{64}Ni_{36}$ experiments in ISS-EML using the VFT viscosity fit over the cooling range of cycle 29. The oscillating heater current is 55.7 A and the oscillating positioner current is 191.7 A.

10.3 Conclusions

Computational fluid dynamics models were analyzed to characterize the flow and shear-strain behavior in electromagnetic-levitation experiments on $Zr_{64}Ni_{36}$ in the ISS-EML facility. At the time of recalescence, flow within the sample was laminar for all 5 cycles analyzed; however, the cycles that had an applied heater voltage during the cooling phase of the cycle were initially turbulent and then crossed the laminar-turbulent transition during the cooling phase of the cycle. Additionally, at recalescence, the shear-strain rate was not within the specifications given in the Science Requirement Document for $Ti_{39.5}Zr_{39.5}Ni_{21}$. Furthermore, the $Zr_{64}Ni_{36}$ sample had cooled at significantly slower rates than were specified for $Ti_{39.5}Zr_{39.5}Ni_{21}$. Calculations should be done for $Zr_{64}Ni_{36}$ at this lower cooling rate to reassess the targeted shear-strain rate and ensure the concentration profiles around subcritical nuclei did not interact during the experiment.

CHAPTER 11

CONCLUSIONS

Computational fluid dynamics models were used to analyze the internal flow of a wide range of microgravity levitation experiments conducted in the ISS-EML facility. This includes an experiment investigating anomalous solidification behavior in an aluminum-nickel alloy, as well as viscosity measurements of molten germanium. In addition, the flow during nucleation experiments was analyzed for Ti39.5Zr39.5Ni21, Cu50Zr50, Vit106, and Zr64Ni36. Each of the experiments had unique set of experimental parameters and requirements, and as a result was calculated to be characterized by different flow behaviors. By analyzing the magnetohydrodynamics of six unique levitation experiments in microgravity, this work had demonstrated that CFD is a valuable approach to gaining critical insight into the fluid flow of molten metal samples.

CHAPTER 12

FUTURE WORK

The continued work on this project will consist of running simulations to support and analyze the flow conditions in ISS-EML experiments. This will include analyzing the flow conditions in a pure zirconium sample that was processed in August 2018 to support studies investigating a solidification phenomenon. In addition, collaborators have requested analysis of samples on recently completed and upcoming campaigns on the ISS.

12.1 Zirconium

The first sample to be analyzed is the zirconium sample processed in batch 1.3 of the ISS-EML experiments. This sample was originally processed in Batch 1.2 to explore the density, thermal transport measurements, surface tension, viscosity and undercooling as a function of cooling rate [64]. During these initial experiments, the sample displayed interesting and unexpected behavior when holding at an undercooling insufficient to induce solidification at which the

Table 18: Targeted undercooling and applied heater control voltage during ISS MSL-EML experiments on Zirconium solidification.

Undercooling (ΔT)°C	Heater Control Voltage (V)
Free Cooling	0.000
25	4.919
50	4.768
100	4.458
185	4.007
225	3.706
275	3.426

sample should have remained liquid but instead solidified.

Further experiments were done in August 2018 as part of batch 1.3 to observe the effects of different undercooling temperatures and the time that the samples would hold at the given temperature before solidifying. The targeted undercooling and corresponding control voltage for the heater coil for these experiments are given in Table 18.

To aid the solidification studies investigating the solidification phenomenon, this proposal proposes to run fluid flow simulations on the zirconium sample at the maximum temperature conditions and for each of the undercoolings at the hold temperature. If the flow is laminar under the maximum flow conditions, the maximum flow conditions and flow before recalescence is all that is needed. However, if the flow is turbulent under maximum flow conditions, it will be necessary to determine when or if the flow transitions to laminar during cooling and before recalescence. The models will allow for more accurate characterization of the flow behavior by calculating the flow velocity which is required for Reynolds number calculations. Solving the models also allows the pressure and pressure gradient within the drop to be calculated. The measurements and calculations will help to determine whether or not there is a relationship between the undercooling phenomenon and the conditions within the liquid drop like cavitation, internal flow, and turbulence. It has been theorized that when a cavity in a liquid collapses, the resulting pressure wave causes the melting temperature to spike which results in solidification of the undercooled liquid [71], [72]. The calculations will provide a qualitative basis to compare the experimental results with theory.

BIBLOGRAPHY

[1] H.-J. Fecht and R. K. Wunderlich, "Fundamentals of Liquid Processing in Low Earth Orbit: From Thermophysical Properties to Microstructure Formation in Metallic Alloys," *JOM*, vol. 69, no. 8, pp. 1261–1268, Aug. 2017.

[2] H. Fukuyama and Y. Waseda, *High-Temperature Measurements of Materials*. Springer Science & Business Media, 2008.

[3] D. Furrer and H. Fecht, "Ni-based superalloys for turbine discs," *JOM*, vol. 51, no. 1, pp. 14–17, Jan. 1999.

[4] S. Romano, A. Brandão, J. Gumpinger, M. Gschweitl, and S. Beretta, "Qualification of AM parts: Extreme value statistics applied to tomographic measurements," *Mater. Des.*, vol. 131, no. Supplement C, pp. 32–48, Oct. 2017.

[5] Lord Rayleigh, "On the Capillary Phenomena of Jets," *Proc. R. Soc. Lond.*, vol. 29, no. 196–199, pp. 71–97, Jan. 1879.

[6] D. M. Matson *et al.*, "Use of Thermophysical Properties to Select and Control Convection During Rapid Solidification of Steel Alloys Using Electromagnetic Levitation on the Space Station," *JOM*, vol. 69, no. 8, pp. 1311–1318, Aug. 2017.

[7] R. W. Hyers, D. M. Matson, K. F. Kelton, and J. R. Rogers, "Convection in Containerless Processing," *Ann. N. Y. Acad. Sci.*, vol. 1027, no. 1, pp. 474–494, Nov. 2004.

[8] D. M. Herlach and D. M. Matson, "Nucleation Within the Mushy Zone," in *Solidification of Containerless Undercooled Melts*, 5th Ed., Wiley-VCH, 2012, pp. 213–238.

[9] R. Hyers, D. M. Matson, F. Kelton K, D. Holland-Mortiz, and T. Volkmann, "Fluid-flow effects on phase selection and nucleation in undercooled liquid metals," *J. Phys. Conf. Ser.*, vol. 327, p. 012013, Dec. 2011.

[10] esa, "Material Science Laboratory Electromagnetic Levitator (MSL-EML)," *European Space Agency*. [Online]. Available: http://www.esa.int/Our_Activities/Human_Spaceflight/International_Space_Station/Material_Science_Laboratory_Electromagnetic_Levitator_MSL-EML. [Accessed: 20-Aug-2018].

[11] R. W. Hyers, "Fluid flow effects in levitated droplets," *Meas. Sci. Technol.*, vol. 16, no. 2, pp. 394–401, Feb. 2005.

[12] H. Lamb, "On the Oscillations of a Viscous Spheroid," *Proc. Lond. Math. Soc.*, vol. s1-13, no. 1, pp. 51–70, Nov. 1881.

[13] W. h. Reid, “The oscillations of a viscous liquid drop,” *Q. Appl. Math.*, vol. 18, no. 1, pp. 86–89, Apr. 1960.

[14] P. V. R. Suryanarayana and Y. Bayazitoglu, “Surface tension and viscosity from damped free oscillations of viscous droplets,” *Int. J. Thermophys.*, vol. 12, no. 1, pp. 137–151, Jan. 1991.

[15] X. Xiao, R. W. Hyers, R. K. Wunderlich, H.-J. Fecht, and D. M. Matson, “Deformation induced frequency shifts of oscillating droplets during molten metal surface tension measurement,” *Appl. Phys. Lett.*, vol. 113, no. 1, p. 011903, Jul. 2018.

[16] R. W. Hyers, G. Trapaga, and B. Abedian, “Laminar-turbulent transition in an electromagnetically levitated droplet,” *Metall. Mater. Trans. B*, vol. 34, no. 1, pp. 29–36, 2003.

[17] K. F. Kelton, “Crystal Nucleation in Liquids and Glasses,” in *Solid State Physics*, vol. 45, H. Ehrenreich and D. Turnbull, Eds. Academic Press, 1991, pp. 75–177.

[18] K. F. Kelton, “Kinetic model for nucleation in partitioning systems,” *J. Non-Cryst. Solids*, vol. 274, no. 1, pp. 147–154, Sep. 2000.

[19] K. F. G. Kelton, “Studies of Nucleation and Growth, Specific Heat and Viscosity of Undercooled Melts of Quasicrystals and Polytetrahedral-Phase-Forming Alloys,” presented at the 2002 NASA Materials Science Conference, Huntsville, AL, United States, 2002.

[20] A. B. Hanlon, D. M. Matson, and R. W. Hyers, “Internal convective effects on the lifetime of the metastable phase undercooled Fe–Cr–Ni alloys,” *Philos. Mag. Lett.*, vol. 86, no. 3, pp. 165–174, Mar. 2006.

[21] A. B. Hanlon, D. M. Matson, and R. W. Hyers, “Microgravity Experiments on the Effect of Internal Flow on Solidification of Fe-Cr-Ni Stainless Steels,” *Ann. N. Y. Acad. Sci.*, vol. 1077, no. 1, pp. 33–48, Sep. 2006.

[22] D. A. Porter and K. E. Easterling, *Phase Transformations in Metals and Alloys*. Boston, MA: Springer US, 1992.

[23] R. Lengsdorf, D. Holland-Moritz, and D. M. Herlach, “Anomalous dendrite growth in undercooled melts of Al–Ni alloys in relation to results obtained in reduced gravity,” *Scr. Mater.*, vol. 62, no. 6, pp. 365–367, Mar. 2010.

[24] O. Zikanov, *Essential Computational Fluid Dynamics*. Hoboken, N.J: John Wiley & Sons, Inc., 2010.

[25] J. F. Wendt, J. D. Anderson, and Von Karman Institute for Fluid Dynamics, Eds., *Computational fluid dynamics: an introduction*, 3rd ed. Berlin ; [London]: Springer, 2008.

[26] P. K. Kundu, I. M. Cohen, and D. R. Dowling, *Fluid Mechanics*, 6th ed. Amsterdam, Boston, Heidelberg, London, New York, Oxford, Paris, San Diego, San Franciso, Singapore, Sydney, Tokyo: Academic Press, 2016.

[27] David C. Wilcox, *Basic Fluid Mechanics*, Fourth. DCW Industries, Inc, 2010.

[28] "ANSYS FLUENT 12.0 Theory Guide - 18. Solver Theory." [Online]. Available: http://www.afs.enea.it/project/neptunius/docs/fluent/html/th/node359.htm. [Accessed: 30-Aug-2018].

[29] S. Berry, R. W. Hyers, B. Abedian, and L. M. Racz, "Modeling of turbulent flow in electromagnetically levitated metal droplets," *Metall. Mater. Trans. B*, vol. 31, no. 1, pp. 171–178, Feb. 2000.

[30] N. El-Kaddah and J. Szekely, "The electromagnetic force field, fluid flow field, and temperature profiles in levitated metal droplets," *Metall. Trans. B*, vol. 14, no. 3, pp. 401–410, Sep. 1983.

[31] "4.3.2. RNG k-ε Model." [Online]. Available: https://www.sharcnet.ca/Software/Ansys/16.2.3/en-us/help/flu_th/flu_th_sec_turb_rng.html. [Accessed: 30-Aug-2018].

[32] V. Yakhot and S. A. Orszag, "Renormalization group analysis of turbulence. I. Basic theory," *J. Sci. Comput.*, vol. 1, no. 1, pp. 3–51, Mar. 1986.

[33] J. Lee, D. M. Matson, S. Binder, M. Kolbe, D. Herlach, and R. W. Hyers, "Magnetohydrodynamic Modeling and Experimental Validation of Convection Inside Electromagnetically Levitated Co-Cu Droplets," *Metall. Mater. Trans. B*, vol. 45, no. 3, pp. 1018–1023, Jun. 2014.

[34] J. C. Zong, J. Szekely, and E. Schwartz, "An Improved Computational Technique for Calculating Electromagne : iz Forces and Power Absorptions Generated in Spherical and Deformed Body in Levitation Melting Devices."

[35] R. W. Hyers, "Modeling of and experiments on electromagnetic levitation for materials processing," Massachusetts Institute of Technology, 1998.

[36] "FLUENT 6.3 User's Guide - 25.9.1 Choosing the Pressure-Velocity Coupling Method." [Online]. Available: https://www.sharcnet.ca/Software/Fluent6/html/ug/node1021.htm. [Accessed: 12-Feb-2019].

[37] D. Voss, "SCI-ESA-HSO-ESR-EML2," no. 1, p. 142.

[38] I. Egry *et al.*, "Thermophysical properties of liquid Al-Ni alloys," *High Temp.-High Press.*, vol. 38, no. 4, pp. 343–351, 2010.

[39] L. Skinner and A. C. Barnes, “An oscillating coil system for contactless electrical conductivity measurements of aerodynamically levitated melts,” *Rev. Sci. Instrum.*, vol. 77, no. 12, p. 123904, Dec. 2006.

[40] T. Iida and R. I. L. Guthrie, *The Physical Properties of Liquid Metals*. New York: Oxford University Press, 1988.

[41] Y. Luo *et al.*, “Contactless processing of SiGe-melts in EML under reduced gravity,” *Npj Microgravity*, vol. 2, no. 1, Dec. 2016.

[42] Y. Luo, Damaschke, B., and K. Samwer, “Germanium on the ISS 2017,” presented at the 16th ISS-EML Investigators’ Working Group Meeting, Noordwijk, Netherlands, 29-Aug-2017.

[43] S. Gruner, J. Marczinke, and W. Hoyer, “Short-range order and dynamic viscosity of liquid Cu–Ge alloys,” *J. Non-Cryst. Solids*, vol. 355, no. 14, pp. 880–884, Jun. 2009.

[44] M. J. Assael, I. J. Armyra, J. Brillo, S. V. Stankus, J. Wu, and W. A. Wakeham, “Reference Data for the Density and Viscosity of Liquid Cadmium, Cobalt, Gallium, Indium, Mercury, Silicon, Thallium, and Zinc,” *J. Phys. Chem. Ref. Data*, vol. 41, no. 3, p. 033101, Sep. 2012.

[45] H. Sasaki, E. Tokizaki, X. M. Huang, K. Terashima, and S. Kimura, “Temperature Dependence of the Viscosity of Molten Silicon Measured by the Oscillating Cup Method,” *Jpn. J. Appl. Phys.*, vol. 34, no. 7R, p. 3432, Jul. 1995.

[46] Y. Sato *et al.*, “Viscosity of molten silicon and the factors affecting measurement,” *J. Cryst. Growth*, vol. 249, no. 3, pp. 404–415, Mar. 2003.

[47] G. W. Lee *et al.*, “Link between liquid structure and the nucleation barrier for icosahedral quasicrystal, polytetrahedral, and simple crystalline phases in $\mathrm{Ti}\text{\ensuremath{-}}\mathrm{Zr}\text{\ensuremath{-}}\mathrm{Ni}$ alloys: Verification of Frank’s hypothesis,” *Phys. Rev. B*, vol. 72, no. 17, p. 174107, Nov. 2005.

[48] G. W. Lee, A. K. Gangopadhyay, and K. F. Kelton, “Phase diagram studies of Ti–Zr–Ni alloys containing less than 40at.% Ni and estimated critical cooling rate for icosahedral quasicrystal formation from the liquid,” *Acta Mater.*, vol. 59, no. 12, pp. 4964–4973, Jul. 2011.

[49] R. G. Hennig, K. F. Kelton, A. E. Carlsson, and C. L. Henley, “Structure of the icosahedral Ti-Zr-Ni quasicrystal,” *Phys. Rev. B*, vol. 67, no. 13, p. 134202, Apr. 2003.

[50] K. F. Kelton, “Kinetic model for nucleation in partitioning systems,” *J. Non-Cryst. Solids*, vol. 274, no. 1, pp. 147–154, Sep. 2000.

[51] J. Diao, R. Salazar, K. F. Kelton, and L. D. Gelb, “Impact of diffusion on concentration profiles around near-critical nuclei and implications for theories of nucleation and growth,” *Acta Mater.*, vol. 56, no. 11, pp. 2585–2591, Jun. 2008.

[52] G. P. Bracker and R. W. Hyers, “Calculated Results for Flow Characterization of Ti39.5Zr39.5Ni21 during EML Experiments in Reduced Gravity,” University of Massachusetts, Amherst, Amherst, MA, Apr. 2019.

[53] D. Van Hoesen, “Private Communication,” 13-Oct-2017.

[54] R. C. Bradshaw *et al.*, “Nonlinearities in the undercooled properties of $Ti_{39.5}Zr_{39.5}Ni_{21}$,” *Philos. Mag.*, vol. 86, no. 3–5, pp. 341–347, Jan. 2006.

[55] K. Kelton, A. Gangopadhyay, R. W. Hyers, and D. Holland-Moritz, “Science Requirements Document STUDIES OF NUCLEATION AND GROWTH SPECIFIC HEAT AND VISCOSITY OF UNDERCOOLED MELTS OF QUASICRYSTALS AND POLYTETRAHEDRAL-PHASE-FORMING-ALLOYS.” National Aeronautics and Space Administration, Dec-2003.

[56] P. Galenko *et al.*, “Solidification kinetics of a Cu-Zr alloy: ground-based and microgravity experiments,” *IOP Conf. Ser. Mater. Sci. Eng.*, vol. 192, p. 012028, Apr. 2017.

[57] M. Mohr *et al.*, “Surface Tension and Viscosity of Cu50Zr50 Measured by the Oscillating Drop Technique on Board the International Space Station,” *Microgravity Sci. Technol.*, vol. 31, no. 2, pp. 177–184, Apr. 2019.

[58] K. F. Kelton, “Liquid structure and long range diffusion: Their impact on glass formation and nanoscale devitrification,” *Intermetallics*, vol. 14, no. 8, pp. 966–971, Aug. 2006.

[59] M. E. Blodgett, T. Egami, Z. Nussinov, and K. F. Kelton, “Proposal for universality in the viscosity of metallic liquids,” *Sci. Rep.*, vol. 5, p. 13837, Sep. 2015.

[60] “Liquidmetal Coatings Material,” 31-Jan-2009. [Online]. Available: https://web.archive.org/web/20090131225945/http://coatings.liquidmetal.com/our.material.asp. [Accessed: 25-Jul-2019].

[61] A. Peker and W. L. Johnson, “A highly processable metallic glass: Zr41.2Ti13.8Cu12.5Ni10.0Be22.5,” *Appl. Phys. Lett.*, vol. 63, no. 17, pp. 2342–2344, Oct. 1993.

[62] “Liquidmetal,” *Wikipedia*. 18-May-2019.

[63] J. C. Bendert, M. E. Blodgett, A. K. Gangopadhyay, and K. F. Kelton, “Measurements of volume, thermal expansion, and specific heat in

Zr57Cu15.4Ni12.6Al10Nb5 and Zr58.5Cu15.6Ni12.8Al10.3Nb2.8 liquids and glasses," *Appl. Phys. Lett.*, vol. 102, no. 21, p. 211913, May 2013.

[64] D. Voss, "SCI-ESA-HSO-ESR-EML1," no. 5, p. 139.

[65] G. P. Bracker and R. W. Hyers, "Calculated Flow Characterization for ISS-EML Experiments on Vit106," University of Massachusetts, Amherst, Amherst, MA, Apr. 2019.

[66] M. Sellers, "Private Communication," 26-Mar-2019.

[67] M. E. Blodgett, T. Egami, Z. Nussinov, and K. F. Kelton, "Proposal for universality in the viscosity of metallic liquids," *Sci. Rep.*, vol. 5, no. 1, Nov. 2015.

[68] N. A. Mauro *et al.*, "Electrostatic levitation facility optimized for neutron diffraction studies of high temperature liquids at a spallation neutron source," *Rev. Sci. Instrum.*, vol. 87, no. 1, p. 013904, Jan. 2016.

[69] G. P. Bracker and R. W. Hyers, "Calculated Flow Characterization for ISS-EML Experiments on Zr64Ni36," University of Massachusetts, Amherst, Amherst, MA, Jun. 2019.

[70] R. W. Hyers, G. Trapaga, and B. Abedian, "Laminar-turbulent transition in an electromagnetically levitated droplet," *Metall. Mater. Trans. B*, vol. 34, no. 1, pp. 29–36, Feb. 2003.

[71] W. H. Hofmeister, R. J. Bayuzick, R. Hyers, and G. Trapaga, "Cavitation-induced nucleation of zirconium in low earth orbit," *Appl. Phys. Lett.*, vol. 74, no. 18, pp. 2711–2713, May 1999.

[72] J. D. Hunt and K. A. Jackson, "Nucleation of Solid in an Undercooled Liquid by Cavitation," *J. Appl. Phys.*, vol. 37, no. 1, pp. 254–257, Jan. 1966.